The University of Maine
DigitalCommons@UMaine

Honors College

Summer 8-2013

A Lateral Field Excited Thin Film Bulk Acoustic Wave Sensor

Michael R. FitzGerald
University of Maine

Follow this and additional works at: https://digitalcommons.library.umaine.edu/honors

Part of the Mathematics Commons, and the Physics Commons

Recommended Citation
FitzGerald, Michael R., "A Lateral Field Excited Thin Film Bulk Acoustic Wave Sensor" (2013). *Honors College*. 631.
https://digitalcommons.library.umaine.edu/honors/631

This Honors Thesis is brought to you for free and open access by DigitalCommons@UMaine. It has been accepted for inclusion in Honors College by an authorized administrator of DigitalCommons@UMaine. For more information, please contact um.library.technical.services@maine.edu.

A LATERAL FIELD EXCITED THIN FILM BULK ACOUSTIC WAVE SENSOR

by

Michael R. FitzGerald

A Thesis Submitted in Partial Fulfillment
of the Requirements for a Degree with Honors
(Physics and Mathematics)

The Honors College

University of Maine

August 2013

Advisory Committee:

John Vetelino, Professor of Electrical and Computer Engineering, Advisor
Nuri Emanetoglu, Associate Professor of Electrical and Computer Engineering
David Frankel, Senior Research Scientist, LASST
Andre Khalil, Associate Professor of Mathematics
Mark Haggerty, Rezendes Preceptor for Civic Engagement, Honors College

ABSTRACT

Medical and environmental needs have served as a catalyst for the development of sensors that can probe the molecular level and below. This study addresses the practicality of highly sensitive aluminum nitride (AlN) thin film bulk acoustic wave resonators (FBARs) as sensors from theoretical and experimental points of view. Theoretically, COMSOL Multiphysics simulations predict that lateral field excitation of AlN produces an electric field perpendicular to the c-axis, with the electrical energy density being concentrated in the active area of the sensor. An analysis of the piezoelectrically stiffened Christoffel equation shows that the shear mode can be excited by an applied electric field in the $x - y$ plane. Several thin films were deposited on various substrates such as borosilicate glass, silicon, sapphire, and fused silica using RF reactive magnetron sputtering and e-beam evaporation. To characterize film structure and composition, x-ray diffraction and x-ray photoelectron spectroscopy were used. An Agilent network analyzer was used to assess the performance of the sensor in air and water.In the most successful case, c-axis AlN films with a FWHM of 1.5 degrees were fabricated with quality factors between 33-36 in air and water. The magnitude of the admittance did not change appreciably when the film was exposed to water, indicating a shear mode was excited. Overall, a building block to a realizable AlN sensor was established.

ACKNOWLEDGMENTS

This work could not have been completed without the generous support of the National Science Foundation and their Research Experience for Undergraduates program. I would also like to thank my advisor, Professor John Vetelino, for his constant support and guidance throughout this project. In addition, I thank my committee members for technical guidance and their constant availability.

TABLE OF CONTENTS

1 Introduction **1**

1.1 Background 1

1.2 Acoustic Sensors 3

1.3 Other Methods of Sensing 5

1.4 Motivation 7

1.5 Outline 8

2 Theory **9**

2.1 Classical Electrodynamics 9

2.2 Acoustic Waves 12

2.3 Stress and Strain in One Dimension 14

2.3.1 One-Dimensional Acoustic Wave Equation 17

2.3.2 Power 18

2.4 Stress and Strain in Three Dimensions 18

2.4.1 Christoffel Equation 24

2.5 Piezoelectricity 25

2.6 Plane Waves in Piezoelectric Solids 27

2.7 Quasistatic Approximation 29

2.8 Wave Analysis 31

2.9 Symmetry Considerations 32

2.10 Finite Element Modeling 35

3 Materials and Methods **40**

3.1 AlN 40

3.2 AlN Material Constants 41

3.3 Butterworth Van-Dyke Equivalent Circuit 41

3.4 Quality Factor 43

3.5 Chemical Bond of AlN 44
3.6 RF Magnetron Sputtering 45
3.6.1 Parameters 47
3.7 Growth 47
3.8 E-beam evaporation 48
3.9 Photolithography 49
3.10 Structure and X-ray Diffraction 50
3.11 Defects 51
3.12 X-ray Photoelectron Spectroscopy 51
3.13 Network Analyzer 52

4 Results 53

4.1 X-ray Diffraction Results Using RF Magnetron Sputtered Films 53
4.2 Network Analyzer Measurements of Magnetron Sputtered Samples . . . 56
4.3 E-beam Evaporation Measurements: 57
4.4 Network Analyzer Measurements of E-beam Evaporated Samples . . . 59

5 Discussion 62

5.1 RF Magnetron Sputtering 62
5.2 E-beam Evaporation 63

6 Conclusions 65

7 Future Work 66

7.1 Crystallinity 66
7.2 Electrode Configuration 66
7.3 Minimizing Acoustic Interference 67
7.4 Stress 68
7.5 CMOS Integration 68

8 References 69

A Tensors and Indicial Notation **74**

A.1 Tensor Transformations 75

9 Author's Biography **77**

LIST OF FIGURES

1	Block Diagram of the Sensor System	2
2	TFE and LFE Methods	4
3	Electric (left) and Magnetic (right) Field Lines	10
4	Types of Waves	13
5	Strain of a String	14
6	Cube With Stresses	19
7	First Three Harmonics	32
8	Electric Field Lines and Energy Density	36
9	COMSOL Magnitude of the Admittance	37
10	Imaginary Part of the Admittance	38
11	Quality Factor	38
12	Modified Butterworth Van-Dyke Circuit	42
13	Bonds of Aluminum Nitride	44
14	Magnetron Sputtering	46
15	Structure Zone Model	48
16	Hexagonal Crystal Unit Cell	50
17	AlN on Borosilicate Glass at 300°C	53
18	AlN on Borosilicate Glass at 400°C	54
19	AlN on Fused Silica at 550°C	54
20	AlN on Fused Silica at 400°C and 300W Power	55
21	002 Pole Figure	55
22	Return Loss of Sputtered AlN on Fused Silica	56
23	Susceptance of Sputtered AlN on Fused Silica	56
24	Return Loss of Sputtered AlN on Fused Silica after Applying Photoresist	57
25	$\theta - 2\theta$ of AlN on Sapphire	57
26	Full-Width at Half-Maximum of Sputtered AlN on Sapphire	58

27 XPS of AlN on Sapphire 58

28 Susceptance of AlN on Sapphire 59

29 Conductance of AlN on Sapphire 59

30 Zoomed Real and Imaginary Parts of the Admittance of AlN on Sapphire . . . 60

31 Water on Edges 60

32 Water Test 61

33 Rotated Coordinate System 75

1 Introduction

Since our origin, human beings used the five traditional senses to retrieve information from the environment. Early scientific pursuit used these senses to observe natural phenomena. As time progressed, the compounded complexity of intellectual inquiry introduced a need for an extension of our senses, as modern aspirations render their capabilities inadequate. For example, we may want to detect sounds outside our hearing range (20Hz-20kHz), electromagnetic phenomena outside our sight range (about 400-700nm), very large bodies (galaxies), or very small objects (atoms). In addition, we sometimes require safe ways of acquiring information, such as detecting certain bacteria or pathogens to inform us of sickness without risking exposure. To accomplish these goals, we require a device capable of detecting and measuring the quantity of interest, and outputting the data to an observer. We call such entities *sensors*.

1.1 Background

A desire to extend the capabilities of our senses, along with advances in the electronic industry, caused the field of sensors to grow exponentially. As a testament to their potential and utility, current sensors can detect and measure a wide spectrum of phenomena. Some of these phenomena include biological (glucose, cholesterol), chemical (concentration), mechanical (mass, force, viscosity), optical (intensity, velocity), or thermal (temperature, thermal conductivity) quantities. The means of detection can involve electromagnetic waves, heat, mechanical displacements, or radioactivity. Indeed, sensors can find application in almost any area, such as healthcare, national security, or environmental protection (Vetelino & Reghu, 2010; Baraton, 2009).

In the biomedical industry, the accurate and rapid detection of biological agents (such as viruses, proteins, bacteria, etc.) in minute concentrations ($\text{ng}\cdot\text{mL}^{-1}$) remains critical for the early detection of several diseases. With progress in genomics and proteomics, biosensors have become crucial to the diagnostic process. As such, the importance of biosensors begets an overview of their operation and structure. Summarizing these details is the *sensor system*:

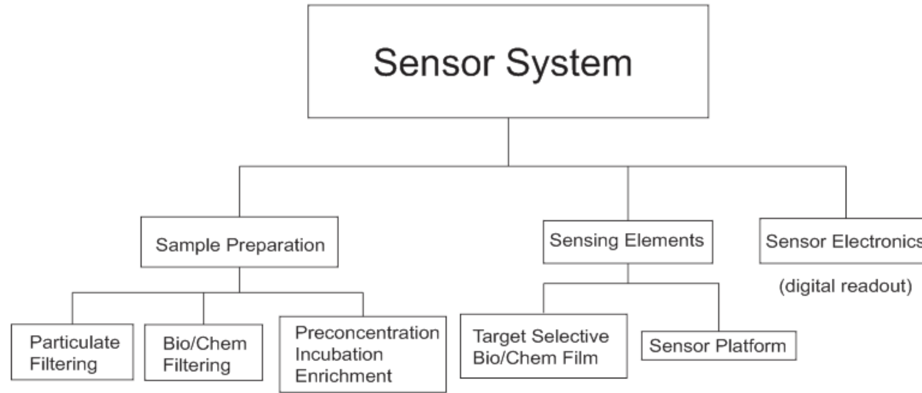

Figure 1: Block Diagram of the Sensor System

The *sensitivity* of a sensor relates to the sensor response per unit measurand. Ideally, the concentration of the measurand and the sensor response should share a direct relationship. *Selectivity* refers to whether or not sensor can respond to a specific measurand. Both of these sensor characteristics can be tuned by sample preparation. For instance, filtering can discard particulates based on size, charge, or other intrinsic properties. The incubation of bacteria allows for an optimal environment for the bacteria to multiply to an appropriate amount before detection occurs. Among many other examples, DNA can be amplified several orders of magnitude through polymerase chain reaction (PCR) in which repetitive heating and cooling melts the extracted DNA, thereafter replicated by enzymes (Mullis & Faloona, 1987).

The second part of the sensor system concerns the detection of the measurand. Sensing platforms, which to a large degree control sensitivity, can be acoustic, electrochemical, magnetic, optical, thermal, or mechanical. Biological or chemical films can be attached to the sensing platform which provide selectivity to the target measurand. Biochemical reactions occur between recognition elements (such as antibodies, antigens, proteins, enzymes, etc.) and the target species. This reaction may produce a measurable change in a physical quantity. A transducer outputs a signal based on these physical perturbations, which can be monitored through a digital readout.

1.2 Acoustic Sensors

Advances in the last fifty years of sensing led to the development of an element known as a bulk acoustic wave (BAW) sensor platform. These sensor platforms consist of two metal electrodes attached to a piezoelectric crystal. The piezoelectric effect, discovered by Jacques and Pierre Curie in 1880, refers to the generation of a voltage in certain materials in response to an applied force ("History of Piezoelectricity," n.d.). A related, but thermodynamically inevitable, consequence of the piezoelectric effect is known as the converse piezoelectric effect. In the converse piezoelectric effect, an applied alternating voltage induces a time-varying strain. As a consequence, piezoelectric crystals can function as capacitors (storing electrical energy with electrodes), motors (applied voltage produces motion), or generators (mechanical energy to electrical energy) (Mason, 1950). In the case of the converse piezoelectric effect, the coupling of the elastic properties of the material and the applied electric field generates an acoustic wave that resonates at certain frequencies. The properties of this wave (velocity, resonant frequency) can change due to interactions between the sensor and its environment. With the assistance of an electrical network analyzer, a device typically monitoring the reflection and transmission of electromagnetic waves, these changes can be monitored through electrical output (impedance or admittance) and the existence of a sensor can be established.

Perhaps the most well-known sensor platform is the quartz crystal resonator, which consists of quartz sandwiched between two metal electrodes. This configuration refers to thickness field excitation (TFE), in which an applied electric field appears along the thickness direction of the material. In the late 1950s, Sauerbrey derived a direct relationship between the resonant frequency and attached mass to a quartz crystal resonator (Sauerbrey, 1959). This device acts like a damped harmonic oscillator, where the losses occur linearly with frequency, and the resonant frequency is inversely proportional to the attached mass. Consequently, quartz had the potential to be used as a gravimetric sensor. As such, it is called a quartz crystal microbalance (QCM). In the 1980s, Kanazawa derived a relationship between the change in oscillation frequency of quartz

in contact with a fluid with its material properties (Kanazawa, 1985). This paper established the ability of the QCM to be a biosensor, and research has been successful in detecting many different chemical or biological entities (Wang, 2010; Carter, 1995; Abad, 1998; Cooper, 2007). Due to its cheapness and durability, the QCM remains a popular choice for sensing applications despite some shortcomings. For instance, the QCM has a relatively low operational frequency (5-20 MHz) due to dimensional restrictions which inhibits its sensitivity (Wingqvist, 2009). Moreover, the QCM is a lumped element, so it cannot be integrated with monolithic circuits. Finally, quartz has a low electromechanical coupling coefficient, or the efficiency of the device to convert mechanical to electrical energy and vice versa.

In contrast to the QCM, Ballato proposed a sensing device utilizing electrodes on one side of the piezoelectric surface, known as lateral field excitation (LFE) in which fringing fields appear along the lateral direction (Hatch & Ballato, 1983). Figure 2 showcases graphical comparison of LFE and TFE devices:

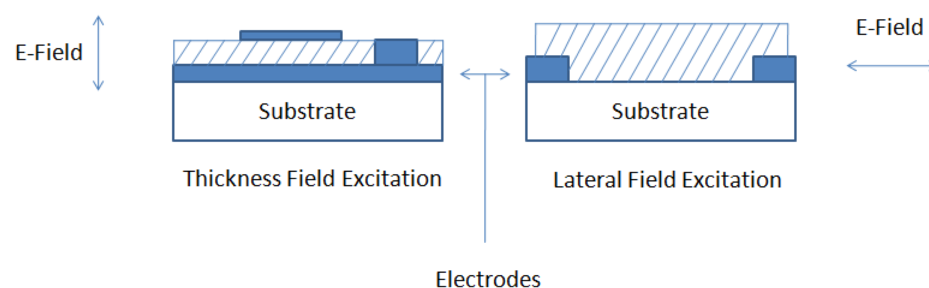

Figure 2: TFE and LFE Methods

At the University of Maine, Vetelino and co-workers were the first to employ this technique to sense a variety of chemical and biological entities, such as saxitoxin, e. coli, or phosmet (Wark, 2007; Hu, 2005; French, 2007). An appealing advantage for an LFE device lies with its bare sensing surface due to the absence of metal on one side. This configuration allows one to sense both mechanical (mass, viscosity, density) or electrical (relative permittivity, conductivity) changes, as no top electrode confines the

electrical energy. Hempel showed that electrical property changes induce a change in the applied electric field (Hempel, 2008), demonstrating LFE devices can have a higher sensitivity than TFE ones. TFEs also cannot excite even harmonics due to electrical boundary conditions of having metal on both sides which prohibits particle displacement. Furthermore, since electrodes can be a source of acoustic scattering, LFE devices can have a higher quality factor than TFEs. Finally, TFEs suffer greater aging because the top electrode lies in the region of greatest vibrational motion (Ballato, 1986). However, TFE sensors experimentally have a higher electromechanical coupling coefficient, so a tradeoff occurs (Wingqvist, 2010). In either case, however, acoustic sensors are label-free (they require no fluorescence or tags), low-cost, and achieve high sensitivity,(Katardjiev and Ventislav, 2012), making them popular choices for sensing.

Acoustic waves can also appear on the surface of devices. Sensors that exploit these waves are called surface acoustic wave (SAW) sensors. These devices consist of interdigital electrodes of alternating voltage sign attached to a piezoelectric crystal. With the proper spacing of electrodes, constructive interference can occur between generated acoustic waves. Although SAW devices have experienced success as biosensors, (Kondoh, 1994; Berkenpas, 2006; Hamamatsu, 1993), their reliance on single-crystal substrates (such as $LiTaO_3$ or $LiNbO_3$) does not allow them to be integrated with circuits such as complementary metal oxide semiconductors (CMOS) (Satoh, 2001).

1.3 Other Methods of Sensing

Other than acoustic transducers, popular methods of detection include enzyme-linked immunosorbent assay (ELISA), (Van Weeman & Schuurs, 1971), surface plasmon resonance (SPR), microcantilever devices, and electrochemical means. The ELISA method includes attaching an antigen to a surface. An antibody binds to the antigen, and a produces a reaction when exposed to the substrate of the enzyme (“ELISA,” n.d.). This reaction can be monitored because it typically produces a color change.

Surface plasmon resonance allows for the detection of analytes by using optical principles. An electromagnetic wave, excited by a light source, is evanescent and prop-

agates along a metal/dielectric interface, which consists of a fluid sample and a recognition element, typically a dielectric that captures certain analytes. When the target measurand is acquired from the fluid sample, the electrical properties of the recognition element change. Using an optical detector, one can measure how the index of refraction of the electromagnetic wave changes, indicating a successful detection of the measurand (Homola, 2008).

Microcantilevers are small beams attached to one side of a mass, leaving the other side free to move. They can be operated in static or dynamic modes, which differ in the response of the beam after the capturing of an analyte by a recognition element. If a microcantilever is in static mode, the displacement of the microcantilever changes due to molecular adsorption which induces surface stresses. On the other hand, a dynamic microcantilever experiences a change in resonant frequency. In either case, the response can be measured with Angstrom resolution (Hansen & Thundat, 2005).

Electrochemical methods include amperometric, voltammetry, and potentiometric methods. Amperometric sensors measure the current between two electrodes after applying a fixed potential. After a redox reaction, the current varies with the concentration of the target measurand. Voltammetric sensors operate in a similar manner to the amperometric sensors, but the voltage is not fixed. Potentiometric sensors measure a potential across an electrode/species interface that develops after a redox reaction occurs (Bronzino, 2000).

Although each of the above methods has many advantages, a key shortcoming concerns how easily these methods can be used for high-throughput detection and the real-time analysis of different measurands. Furthermore, each of the above methods monitors only certain properties. ELISA measures typically color change. SPR sensors measure index of refraction. Microcantilever beams monitor induces stresses. Finally, electrochemical sensors measure current, voltage, or resistance. Increases in sensitivity can be attained by a biosensor platform that measures as many changes occuring as possible due to biolayer and analyte interactions. As previously stated, losses are a linear function of frequency for acoustic sensors. Sensitivity, on the other hand, is

an exponential function of frequency, indicating that thinner devices (and hence greater resonant frequencies) can achieve lower limits of detection than conventional devices. However, thinner devices, and those that are polycrystalline, will require mechanical support in the form of a substrate.

1.4 Motivation

Medical and environmental needs have provided the impetus to develop highly sensitive sensors to probe targets of the molecular level and below. This thesis focuses on the design, fabrication, and testing of a device known as a thin film bulk acoustic resonator (FBAR), consisting of an aluminum nitride (AlN) piezoelectric thin film and aluminum electrodes. FBARs have been used in the telecom industry as filters (devices suppress certain signals), but their sensing potential have not been fully realized. Due to their thickness on the order of 1-3μm, a much higher resonant frequency can be obtained than in QCMs. A brief analysis of the Sauerbrey equation, which relates the material constants of a piezoelectric material, a rigid mass deposited on it, and the change in resonant frequency in the form

$$\Delta f = -\frac{2f_0^2}{A\sqrt{\rho_q \mu_q}}\Delta m, \tag{1.1}$$

where Δf and f_0 refer to the change in frequency and resonant frequency, respectively (Hz), Δm corresponds to the change in mass (g), A is the area between the electrodes (cm^2), ρ_q refers to the density of quartz (g$\cdot$cm^{-3}) and μ_q is the shear modulus of quartz (g$\cdot$cm$^{-1}\cdot$s^{-2}), reveals that these devices can theoretically offer a thousand-fold increase in mass sensitivity over the QCM due to their operational frequency in the GHz range. This figure diminishes experimentally due to the presence of noise factors, but remains around a hundred-fold more sensitive. A primary focus of this project has been exploiting FBARs for sensing purposes using lateral field excitation in liquid-phase. With this fundamental building block established, sensor arrays can be realized, thereby leading to simultaneous measurement of many different quantities of interest.

In the medical industry, for example, biomarkers can be found in human fluid (such as blood, urine, saliva, etc.). Hundreds of biomarkers for cancer have been identified (Polanski & Anderson, 2006).

1.5 Outline

This thesis contains seven chapters. The first chapter presents a cursory overview of BAW sensing and historical developments. Chapter two discusses the theory of acoustic waves in non-piezoelectric and piezoelectric crystals with special attention given towards mechanical and electromagnetic phenomena. A chapter on the materials and methods used can be found in chapter three, including material properties of AlN and brief summaries of the underlying theory of the measuring apparati used to characterize these sensors. Results of testing can be found in chapter 4. Finally, chapters 5, 6 and 7 present the discussion, conclusions, and future work.

2 Theory

This chapter begins with a review of rudimentary electrodynamics. Waves and the wave equation are then examined. Acoustic phenomena such as stress and strain in homogeneous media are discussed. The equations of translational motion and the wave equation are developed in one and three dimensions, emphasizing the parallels between electrodynamics and acoustics. The Christoffel equation is derived. Piezoelectricity is developed as a bridge between mechanical and electrical phenomena, leading to the development of the stiffened Christoffel equation. The chapter ends with a theoretical treatment of AlN FBARs most relevant to this thesis, including symmetry considerations and acoustic waves. Most of the theory follows Auld (1973), Rosenbaum (1988), Tiersten (1969), Nye (1957), and Mason (1950). Boldface variables henceforth indicate vectors.

2.1 Classical Electrodynamics

Positive and negative charges make up most matter. Opposite charges attract, whereas like charges repel. These interactions between charged particles can be described using electric fields. A field is an important concept in physics that assigns a value of a quantity to every spatial and temporal point. An *electric field* emanates radially from a positive charge, the lines of which portray the force felt by a charged particle due to another one. A moving charge generates a *magnetic field*. Figure 1 depicts both fields:

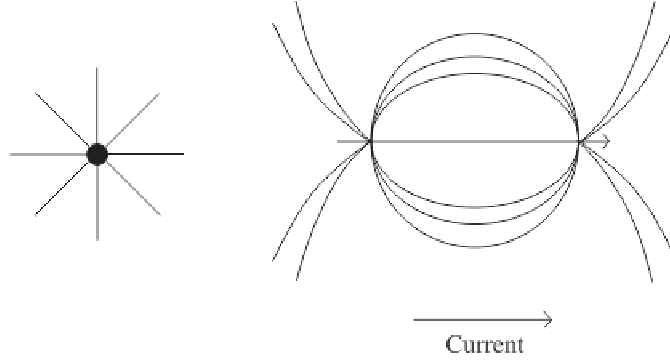

Figure 3: Electric (left) and Magnetic (right) Field Lines

The electromagnetic force between two charged particles can be described by the *Lorentz force*:

$$\mathbf{F} = q\left(\mathbf{E} + \mathbf{v} \times \mathbf{B}\right), \tag{2.1}$$

where $\mathbf{F}$ denotes the force (N), $\mathbf{E}$ is the electric field (V·m^{-1}), q corresponds to the charge of the particle on which the force acts (C), $\mathbf{v}$ is the velocity of the particle (m·s^{-1}), and $\mathbf{B}$ is the magnetic field (T). Electric and magnetic fields in matter are described by the constitutive equations:

$$\mathbf{D} = \epsilon\mathbf{E} + \mathbf{P}, \text{ and } \mathbf{B} = \mu\mathbf{H} + \mathbf{M}, \tag{2.2}$$

where $\mathbf{D}$ is the electrical displacement field (C·m^{-2}), $\mathbf{H}$ refers to the demagnetizing field (A·m^{-1}), and ϵ and μ correspond to the relative permittivity (F·m^{-1}) and permeability (H·m^{-1}) of the material, respectively. $\mathbf{P}$ and $\mathbf{M}$ refer to the polarization and magnetization densities. These refer to the density of induced dipole moments, or the separation of positive and negative charges in a material, and the density of the magnetic dipole moments. Maxwell's equations in flat spacetime, along with the Lorentz force law, provide a theoretical framework for the interactions between charges, currents, and

fields. The Maxwell equations are given below in differential form:

$$\nabla \cdot \mathbf{D} = \rho_e \quad \text{(a)}$$

$$\nabla \cdot \mathbf{B} = 0 \quad \text{(b)}$$

$$\nabla \times \mathbf{E} = -\frac{\partial \mathbf{B}}{\partial t} \quad \text{(c)}$$

$$\nabla \times \mathbf{B} = \mu_0 \epsilon_0 \frac{\partial \mathbf{E}}{\partial t} + \mu_0 \mathbf{J}, \quad \text{(d)}$$

(2.3)

where ρ_e denotes the electrical charge density (C·m^{-3}), ϵ_0 and μ_0 correspond to the permittivity and permeability of free space, with the same units as before, respectively, and $\mathbf{J}$ refers to the current density (A·m^{-2}).

The Poynting vector (W·m^{-2}) can be derived from (2.3) to describe power flow:

$$\mathbf{S} = \mathbf{E} \times \mathbf{H}. \tag{2.4}$$

The divergence of the Poynting vector yields the power of an electromagnetic wave:

$$\nabla \cdot \mathbf{S} = -\frac{\partial}{\partial t}\left(\frac{1}{2}\epsilon E^2 + \frac{1}{2}\mu H^2\right), \tag{2.5}$$

where the first and second terms correspond to electrical and magnetic energy density, respectively. As we shall see later, acoustic phenomena mirrors closely electromagnetic phenomena.

Decoupling Maxwell's equations in a vacuum obtains the electromagnetic wave equation:

$$\frac{\partial^2 \mathbf{E}}{\partial t^2} = \mu_0 \epsilon_0 \nabla^2 \mathbf{E}. \tag{2.6}$$

The solution of this equation in three-space, assuming harmonic time-variation and

absorbing any arbitrary phase factor $e^{j\phi}$ into the constant E_0, is given by:

$$\mathbf{E} = \mathbf{E}_0 e^{j(\mathbf{k}\cdot\mathbf{r} - \omega t)}, \tag{2.7}$$

where **k** denotes the wave-vector (m^{-1}), $\mathbf{r} = l_x\hat{i} + l_y\hat{j} + l_z\hat{k}$ is a position vector. These complex quantities represent oscillating plane waves.

2.2 Acoustic Waves

An important idea in physics is the concept of a "wave." The simplest definition of a wave is a disturbance in space and time that transmits energy. In this section we mostly concern ourselves with mechanical or acoustic waves that propagate through a medium. These waves can occur with their displacements perpendicular or parallel to their direction of propagation. We call these waves *transverse* and *longitudinal* waves, respectively. One can easily visualize the difference by imagining a wave traveling in a rope fixed at both ends (transverse), or a wave in a slinky (longitudinal). Fig. 4 illustrates the difference in a standard Cartesian coordinate system (x, y, and z) where arrows denote the direction of displacements:

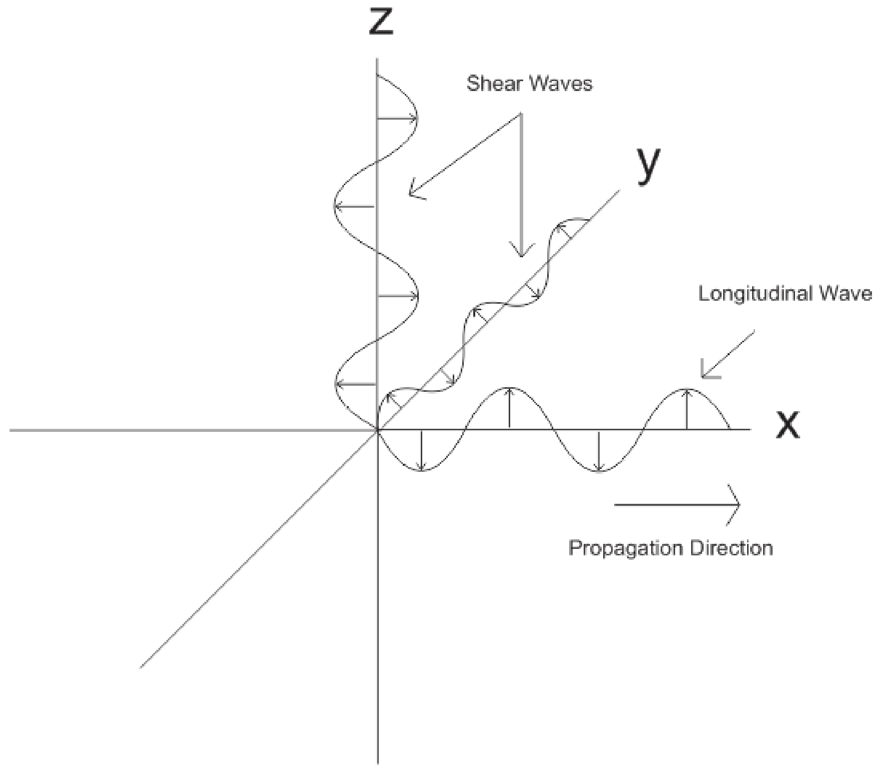

Figure 4: Types of Waves

When discussing bulk acoustic waves, we refer to the longitundal wave as the longitudinal mode, and the transverse waves as shear modes. These modes become important later, as liquid media cannot support shear waves effectively due to their lack of rigidity. For solid materials, their internal structure consists of tightly packed molecules, which induces restoring forces otherwise absent in liquids. For sensing in the liquid-phase, shear modes are required so no energy leaks out to the surroundings from compressional motion.

Theoretically, the wave displacements, $u = f(x, y, z, t)$, are solutions to the following differential equation,

$$\frac{\partial^2 u}{\partial t^2} = c^2 \nabla^2 u, \tag{2.8}$$

where c refers to the speed of the wave (units of m$\cdot$s^{-1}), and $\nabla^2 = (\frac{\partial^2}{\partial x^2} + \frac{\partial^2}{\partial y^2} + \frac{\partial^2}{\partial z^2})$ is the spatial Laplacian operator.

2.3 Stress and Strain in One Dimension

Newton's second law states that the acceleration of an object varies directly with an applied net force and inversely to its mass. Assuming a constant mass, we can symbolically represent this law as:

$$\mathbf{F} = m\mathbf{a}, \tag{2.9}$$

where m represents mass (kg), and **a** corresponds to acceleration (m$\cdot$s^{-2}). Under the assumptions above, a change in force produces a change in acceleration. In the limit of infinitesimal change, we can write (2.9) using differentials:

$$\mathrm{d}\mathbf{F} = m\mathrm{d}\mathbf{a}. \tag{2.10}$$

As seen in (2.9), applying a force to a rigid body causes an acceleration in the direction of the force. This force can manifest itself as a rigid rotation or a rigid translation. Depending on the magnitude of the force, the medium can undergo a deformation which displaces particles relative to one another. The dimensionless quantity strain, S, represents this distortion. Fig. 5 shows a pictoral representation of strain in one dimension:

Figure 5: Strain of a String

Label the origin as O, with a stretchable string A of length z. Let A be stretched a distance of u. The distance from point A to an arbitrary point B on the string will change by a factor $\Delta z + \Delta u$. At the point A, the increase in length over the original length is,

$$\frac{\Delta u}{\Delta z}. \tag{2.11}$$

This is a ratio of increase in length to the original length. The definition of strain,

S, at point A is a limit of (2.11) as z goes to 0:

$$\mathbf{S} = \lim_{\Delta z \to 0} \frac{\Delta \mathbf{u}}{\Delta z} = \frac{\mathrm{d}\mathbf{u}}{\mathrm{d}z}, \tag{2.12}$$

or the spatial rate of change of particle displacement, where both **u** and z have dimensions of length.

A non-strained material is in a state of thermal and mechanical equilibrium (Landau & Lifshitz, 1959). For sufficiently small strains, internal molecular forces attempt to return the material to its equilibrium state. These forces, called stresses, **T**, have units of force per area (N·m^{-2}). The assumption of linearity results in Hooke's Law, where stress and strain are linearly related by a material constant:

$$\mathbf{T} = c\mathbf{S}, \tag{2.13}$$

where c is the elastic stiffness constant of a material with units of N·m^2. Small values of c indicate a pliable material. With a large enough stress, Hooke's law may be rendered invalid, and the material may fracture or crack. For real materials, damping forces appear and modify Hooke's law to yield:

$$\mathbf{T} = c\mathbf{S} + \eta \frac{\mathrm{d}\mathbf{S}}{\mathrm{d}t}, \tag{2.14}$$

where η corresponds to a damping factor. Similarly to (2.13), stress can be the dependent variable by introducing the elastic compliance of a material:

$$\mathbf{S} = s\mathbf{T}, \tag{2.15}$$

where s has units of m^2·N^{-1} and measures how easily the material deforms. Materials with large s values can be easily deformed.

The field of acoustics deals with time-varying strains and stresses in materials. Specifically, it deals with the coupling of stress and strain, where induced stresses combined with inertia of the particles generates oscillatory motion (Auld, 1973). A one-

dimensional wave equation can model this oscillatory motion using the three variables of stress, strain, and particle displacement. Physically, we want to obtain a relationship between the spatial variation of stress with how it varies in time. We can achieve this as follows.

We first note that the first and second time derivatives of particle displacement

$$\mathbf{v} = \frac{\mathrm{d}\mathbf{u}}{\mathrm{d}t}, \ \mathbf{a} = \frac{\mathrm{d}^2\mathbf{u}}{\mathrm{d}t^2} = \frac{\mathrm{d}\mathbf{v}}{\mathrm{d}t}, \tag{2.16}$$

represent particle velocity and acceleration, respectively. Using dimensional analysis, we see that **F** and **T** are related by the area over which the stress is acting by the equation:

$$\mathbf{F} = A\mathbf{T} \implies \mathrm{d}\mathbf{F} = \mathrm{d}A\mathrm{d}\mathbf{T}. \tag{2.17}$$

Finally, we can represent the mass of a body by using its density, ρ (kg·m^{-3}), multiplied by the differential volume it occupies ($\mathrm{d}x\mathrm{d}y\mathrm{d}z$):

$$m = \rho \mathrm{d}x\mathrm{d}y\mathrm{d}z. \tag{2.18}$$

Substituting (2.16-18) into (2.10) yields

$$\mathrm{d}A\mathrm{d}\mathbf{T} = \rho \mathrm{d}x\mathrm{d}y\mathrm{d}z\frac{\partial^2\mathbf{u}}{\partial t^2}. \tag{2.19}$$

Since $\mathrm{d}A$ = $\mathrm{d}x\mathrm{d}y$, (2.19) becomes

$$\mathrm{d}\mathbf{T} = \rho \mathrm{d}z\frac{\partial^2\mathbf{u}}{\partial t^2}. \tag{2.20}$$

Using properties of differentials, we can divide both sides of (2.20) by $\mathrm{d}z$. However, since stress depends on a variety of variables, we to use a partial derivative.

$$\frac{\partial\mathbf{T}}{\partial z} = \rho\frac{\partial^2\mathbf{u}}{\partial t^2}. \tag{2.21}$$

This is the one-dimensional translational equation of motion. We now have an ex-

pression for how stress varies spatially. Obtaining an acoustic wave equation requires a relationship between how stress varies spatially and temporally.

2.3.1 One-Dimensional Acoustic Wave Equation

Taking the time derivative of (2.12) obtains (due to the coupling of stress and strain we appropriately assign a partial derivative to strain)

$$\frac{\partial \mathbf{S}}{\partial t} = \frac{\partial^2 \mathbf{u}}{\partial z \partial t}. \tag{2.22}$$

Substituting (2.13) into (2.22) and assuming the elastic stiffness of the material is constant in time yields

$$\frac{1}{c}\frac{\partial \mathbf{T}}{\partial t} = \frac{\partial^2 \mathbf{u}}{\partial z \partial t}. \tag{2.23}$$

With (2.16), (2.23) becomes

$$\frac{1}{c}\frac{\partial \mathbf{T}}{\partial t} = \frac{\partial \mathbf{v}}{\partial z}. \tag{2.24}$$

Differentiating (2.24) with respect to time and (2.21) with respect to z, and again using the fact that velocity is the temporal variation of particle displacement yields,

$$\frac{1}{c}\frac{\partial^2 \mathbf{T}}{\partial t^2} = \frac{\partial^2 \mathbf{v}}{\partial t \partial z}, \text{ and } \frac{\partial^2 \mathbf{T}}{\partial z^2} = \rho\frac{\partial^2 \mathbf{v}}{\partial t \partial z}, \tag{2.25}$$

respectively.

Finally, equating the two sides of (2.25) obtains

$$\frac{\rho}{c}\frac{\partial^2 \mathbf{T}}{\partial t^2} = \frac{\partial^2 \mathbf{T}}{\partial z^2}. \tag{2.26}$$

Equation (2.26) describes the propagation of an acoustic wave in one dimension. Initial and boundary conditions are required for a unique solution. Careful examination of (2.26) shows that in one dimension, the solution is an acoustically polarized plane wave whose displacements occur in the direction of propagation (longitudinal mode). As we move to three dimensions, three different acoustic polarizations arise.

2.3.2 Power

Using (2.21), (2.22), and Hooke's Law, we can form the analogous power definition:

$$-\frac{\partial}{\partial z}(Tv) = -\frac{\partial}{\partial t}\left(\frac{1}{2}\rho v^2 + \frac{1}{2}cS^2\right) - \frac{1}{2}\frac{\partial}{\partial t}\omega\eta S^2. \tag{2.27}$$

In an acoustic system, energy oscillates between potential and kinetic energy. According to elementary mechanics, the quality factor of a resonator takes on the following form:

$$Q \equiv \frac{\omega(\text{energy stored})}{(\text{energy dissipated})}. \tag{2.28}$$

In this case, the energies stemming from the strain and kinetic parts equal at their maximum, so the quality factor becomes:

$$Q = \frac{c}{\omega\eta} = \frac{v^2\rho}{\omega\eta}. \tag{2.29}$$

This relationship carries over into three-dimensions and piezoelectric resonators.

2.4 Stress and Strain in Three Dimensions

When dealing with acoustic wave propagation in three dimensions, we must use the tensor fields of stress and strain. Each of these fields assigns a second-order tensor to each point in space. The stress tensor is:

$$\begin{bmatrix} T_{11} & T_{12} & T_{13} \\ T_{21} & T_{22} & T_{23} \\ T_{31} & T_{32} & T_{33}. \end{bmatrix} \tag{2.30}$$

The subscripts associated with each stress, T_{ij}, denote the surface (i) on which the stress (j-direction) acts. Figure 3 shows the stresses on an arbitrary cube with differential volume dV = dx_1 dx_2 dx_3:

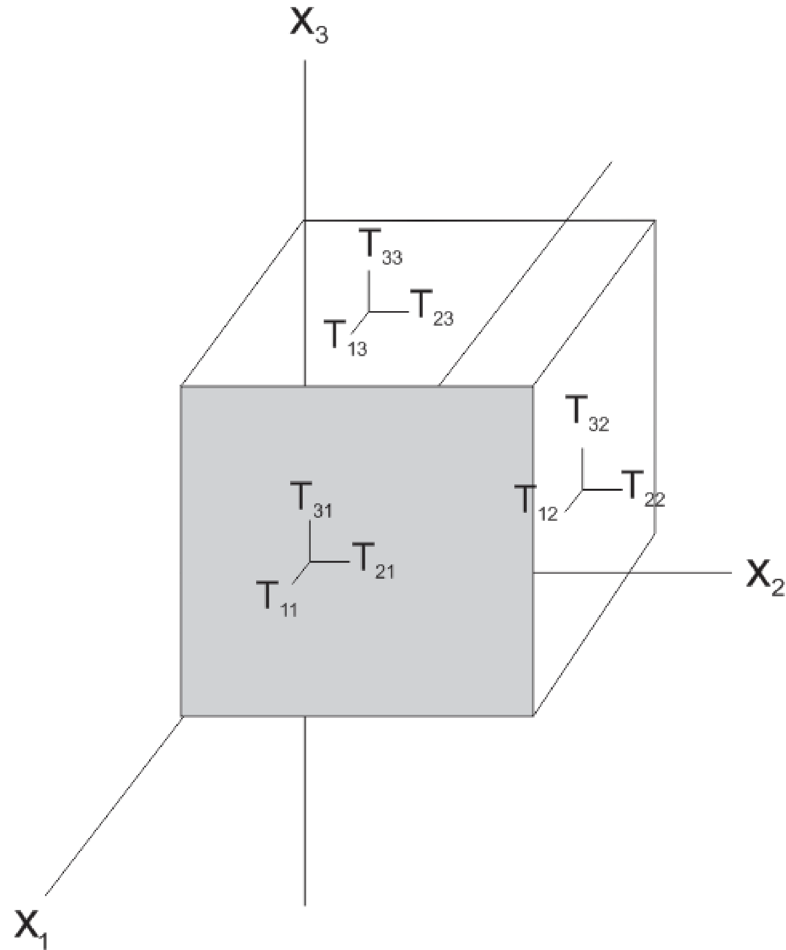

Figure 6: Cube With Stresses

For any surface on that cube, the total stress can be calculated using the sum of the stresses in the x_1, x_2, and x_3 directions. In the case of the shaded surface perpendicular to x_2, we label the stresses in the x_1 and x_3 directions as the shear stresses, T_{21} and T_{31}. The remaining stress, T_{11}, is labeled the longitudinal stress. Shear stresses cut, whereas longitudinal stresses stretch (tensile) or push together (compressional).

The stress tensor is symmetric because there are no applied torques during linear wave propagation. Symbolically we can represent this as $T_{ij} = T_{ji}$. Examining figure 6, we can see that in order for the cube not to spin, the torques around the center must be equal and opposite. Hence, the nine components in (3.16) reduce to six independent

ones and can be represented as a 6×1 matrix:

$$\begin{bmatrix} T_1 \\ T_2 \\ T_3 \\ T_4 \\ T_5 \\ T_6, \end{bmatrix} \tag{2.31}$$

the components of which followed the index transformation, called Voigt notation:

$$T_{ij} = \begin{cases} T_i & \text{if } i = j \\ T_4 & \text{if } ij = 32 \text{ or } 23 \\ T_5 & \text{if } ij = 13 \text{ or } 31 \\ T_6 & \text{if } ij = 12 \text{ or } 21 \end{cases}. \tag{2.32}$$

One useful relationship is the divergence of the stress tensor, which becomes a vector:

$$\nabla \cdot \mathbf{T} = \begin{bmatrix} \frac{\partial}{\partial x}T_1 + \frac{\partial}{\partial y}T_6 + \frac{\partial}{\partial z}T_5 \\ \frac{\partial}{\partial x}T_6 + \frac{\partial}{\partial y}T_2 + \frac{\partial}{\partial z}T_4 \\ \frac{\partial}{\partial x}T_5 + \frac{\partial}{\partial y}T_4 + \frac{\partial}{\partial z}T_3 \end{bmatrix}. \tag{2.33}$$

This can be cast into matrix form:

$$\nabla \cdot \mathbf{T} = \begin{bmatrix} \frac{\partial}{\partial x} & 0 & 0 & 0 & \frac{\partial}{\partial z} & \frac{\partial}{\partial y} \\ 0 & \frac{\partial}{\partial y} & 0 & \frac{\partial}{\partial z} & 0 & \frac{\partial}{\partial x} \\ 0 & 0 & \frac{\partial}{\partial z} & \frac{\partial}{\partial y} & \frac{\partial}{\partial x} & 0 \end{bmatrix} \begin{bmatrix} T_1 \\ T_2 \\ T_3 \\ T_4 \\ T_5 \\ T_6 \end{bmatrix}. \tag{2.34}$$

The matrix divergence operator can be cast into index notation as:

$$\nabla\cdot \implies \nabla_{iJ}, \tag{2.35}$$

where i ranges from 1 to 3 (rows) and J ranges from 1 to 6 (columns).

Since stress usually accompanies strain and vice-versa, we want to establish a matrix form for strain as well. The linearized (*i.e.*, ignoring quadratic terms) strain-displacement equation is constructed from the three-dimensional analogue of (2.12) ($e_{ij} = \frac{\partial u_i}{\partial x_j}$). Any tensor can be decomposed into symmetric and antisymmetric parts, and the strain-displacement equation refers to the symmetric part of it: (piezoelectricity, mason, 445):

$$S_{kl} = \frac{1}{2}\left(\frac{\partial u_k}{\partial r_l} + \frac{\partial u_l}{\partial r_k}\right), \tag{2.36}$$

where k and l range from 1 to 3, r_l and r_k take on the familiar Cartesian coordinates based on which index, and the existence of cross-terms correspond to shear terms in three-dimensions. The antisymmetric part corresponds to rotation and does not concern this thesis. According to (2.36), strain can be represented by a 3×3 matrix. When strain is denoted S_{kl}, the subscripts concern the particle displacement in the k direction with respect to the l direction. Again due to symmetry, there are only six independent components:

$$\begin{bmatrix} S_{11} & S_{12} & S_{13} \\ S_{21} & S_{22} & S_{23} \\ S_{31} & S_{32} & S_{33} \end{bmatrix} \implies \begin{bmatrix} S_1 \\ S_2 \\ S_3 \\ S_4 \\ S_5 \\ S_6 \end{bmatrix} \implies \begin{bmatrix} \frac{\partial}{\partial x} & 0 & 0 \\ 0 & \frac{\partial}{\partial y} & 0 \\ 0 & 0 & \frac{\partial}{\partial z} \\ 0 & \frac{\partial}{\partial z} & \frac{\partial}{\partial y} \\ \frac{\partial}{\partial z} & 0 & \frac{\partial}{\partial z} \\ \frac{\partial}{\partial y} & \frac{\partial}{\partial x} & 0 \end{bmatrix} \begin{bmatrix} u_x \\ u_y \\ u_z \end{bmatrix} = S. \tag{2.37}$$

Evidently, operating on a displacement vector $\mathbf{u} = (u_x, u_y, u_z)$ with the strain matrix

yields the six strain equations:

$$S_1 = \frac{\partial u_x}{\partial x}, \quad S_2 = \frac{\partial u_y}{\partial y}, \quad S_3 = \frac{\partial u_z}{\partial z}. \tag{2.38}$$

$$S_4 = \frac{1}{2}\left(\frac{\partial u_y}{\partial z} + \frac{\partial u_z}{\partial y}\right), \quad S_5 = \frac{1}{2}\left(\frac{\partial u_x}{\partial z} + \frac{\partial u_z}{\partial x}\right), \quad S_6 = \frac{1}{2}\left(\frac{\partial u_x}{\partial y} + \frac{\partial u_y}{\partial x}\right). \tag{2.39}$$

This equation is commonly written as:

$$\mathbf{S} = \nabla_s \mathbf{u} = \nabla_{Ij} \mathbf{u}, \tag{2.40}$$

where I ranges from 1 to 6, and j ranges from 1 to 3. Due to the relationships between stress and strain, the divergence of stress takes on the form as the transpose of ∇_{Ij}.

Hooke's Law can be generalized to three dimensions, where c is now a matrix of elastic stiffness constants. It is a fourth rank tensor and thus has $3^4 = 81$ components. However, due to the symmetry of the stress $T_{ij} = T_{ji}$ and strain tensors $S_{kl} = S_{lk}$, $c_{ijkl} = c_{jikl} = c_{ijlk} = c_{klij}$. Consequently, $s_{ijkl} = s_{ijlk} = s_{jikl} = s_{klij}$. As a result, only 21 components of both matrices are independent. Further symmetry conditions can reduce this number. The units remain N$\cdot$m^{-2}, and the elastic stiffness matrix can be mapped onto a 6$\times$6 matrix:

$$c = \begin{bmatrix} c_{11} & c_{12} & c_{13} & c_{14} & c_{15} & c_{16} \\ c_{21} & c_{22} & c_{23} & c_{24} & c_{25} & c_{26} \\ c_{31} & c_{32} & c_{33} & c_{34} & c_{35} & c_{36} \\ c_{41} & c_{42} & c_{43} & c_{44} & c_{45} & c_{46} \\ c_{51} & c_{52} & c_{53} & c_{54} & c_{55} & c_{56} \\ c_{61} & c_{62} & c_{63} & c_{64} & c_{65} & c_{66} \end{bmatrix}. \tag{2.41}$$

In indicial notation, Hooke's law may be written in a more convenient form:

$$T_{ij} = c_{ijkl} S_{kl}, \tag{2.42}$$

or

$$T = c : S \implies S = s : T. \tag{2.43}$$

This is analogous to the electrical constitutive equation relating electrical displacement and the electric field.

Using the tensor of stress, we can now form a translational equation of motion in three-dimensions. To start, assume we have an arbitrary material with a differential volume $\mathrm{d}V$ and a differential surface area $\mathrm{d}S$. We can rewrite Newton's second law as:

$$\oiint_S \mathbf{T} \cdot \mathbf{n} \, \mathrm{d}S = \frac{\mathrm{d}}{\mathrm{d}t} \iiint_V \rho \mathbf{v} \, \mathrm{d}V, \tag{2.44}$$

where $\mathbf{T} \cdot \mathbf{n}$ computes the contribution of stress on each surface:

$$\mathbf{T} \cdot \mathbf{n} = \begin{bmatrix} T_x & T_y & T_z \end{bmatrix} \begin{bmatrix} n_x \\ n_y \\ n_z \end{bmatrix}. \tag{2.45}$$

Using the divergence theorem on (2.44) gives us

$$\iiint_V \nabla \cdot \mathbf{T} \, \mathrm{d}V = \iiint_V \rho \frac{\mathrm{d}\mathbf{v}}{\mathrm{d}t} \, \mathrm{d}V. \tag{2.46}$$

Since the volume is arbitrary, we can remove the integrals from (2.46) leaving us with the three-dimensional stress equation of motion:

$$\nabla \cdot \mathbf{T} = \rho \frac{\mathrm{d}\mathbf{v}}{\mathrm{d}t}. \tag{2.47}$$

Please note that the divergence of a second-order tensor is a vector, leaving (2.47) completely consistent.

2.4.1 Christoffel Equation

Recall the constitutive equations

$$\nabla \cdot \mathbf{T} = \rho \frac{d\mathbf{v}}{dt}, \tag{2.48}$$

and

$$\nabla_s \mathbf{u} = \mathbf{S}. \tag{2.49}$$

Taking the time derivative of both sides of (2.49) yields:

$$\nabla_s \mathbf{v} = \frac{\partial \mathbf{S}}{\partial t}. \tag{2.50}$$

Simplifying using (2.43):

$$\nabla_s \mathbf{v} = s : \frac{\partial \mathbf{T}}{\partial t}. \tag{2.51}$$

Equations (2.48) and (2.51) contain spatial and temporal derivatives of $\mathbf{v}$ proportional to the stress field $\mathbf{T}$. Differentiating (2.48) with respect to t yields:

$$\nabla \cdot \frac{\partial \mathbf{T}}{\partial t} = \rho \frac{\partial^2 \mathbf{v}}{\partial t^2}. \tag{2.52}$$

Multiplying (2.51) by the stiffness matrix yields:

$$\mathbf{c} : \nabla_s \mathbf{v} = \frac{\partial \mathbf{T}}{\partial t}. \tag{2.53}$$

Substituting (2.53) into (2.52) obtains the well-known Christoffel equation:

$$\nabla \cdot \mathbf{c} : \nabla_s \mathbf{v} = \rho \frac{\partial^2 \mathbf{v}}{\partial t^2}. \tag{2.54}$$

Using (2.35) and (2.40), and noting that the indices of c must be the same, (2.54) becomes:

$$\nabla_{iJ} c_{JI} \nabla_{Ij} v_j = \rho \frac{\partial^2 v_i}{\partial t^2}. \tag{2.55}$$

Consider a plane wave propagating in the l direction, given by:

$$\mathbf{l} = (l_x, l_y, l_z). \tag{2.56}$$

$\mathbf{v}$ is proportional to:

$$v \propto e^{j(\omega t - k\mathbf{l}\cdot\mathbf{r})} = e^{j(\omega t - k(l_x x + l_y y + l_z z))}, \tag{2.57}$$

similar to the electromagnetic case. In this case, energy is transferred between strain and particle velocity, analogous to a mass and a spring system where energy is divided between potential and kinetic energy. Performing spatial derivatives on (2.57) allows one to rewrite the divergence and gradient operators in a more convenient form:

$$\nabla_{iJ} \to -jkl_{iJ} \text{ and } \nabla_{Ij} \to -jkl_{Ij}. \tag{2.58}$$

These identities can cast (2.55) in a more appeasing form:

$$-k^2\Gamma_{ij}v_j = -\rho\omega^2 v_i, \tag{2.59}$$

where the *Christoffel matrix* is:

$$\Gamma_{ij} = l_{iJ}c_{JI}l_{Ij}. \tag{2.60}$$

Equation (2.59) is an eigenvalue equation, where a linear operator acting on a vector returns the same vector, just stretched by a constant. The eigenvectors of this equation correspond to the velocities of the particles whose eigenvalues relate to the phase velocities.

2.5 Piezoelectricity

Now that the foundation of acoustic waves has been established, we now extend the theory to include electromagnetic effects. Piezoelectricity occurs in crystals that do not

have a center of symmetry. These crystals may either be polar, where a total dipole moment exists in the crystal, or non-polar, where the centers of gravity for the positive and negative charges coincide somewhere other than the center of the cell. Two related effects of piezoelectricity occur: The direct piezoelectric effect, and the converse piezoelectric effect. The former occurs when a strain produces bound charges in a material, whereas the latter occurs when an applied electric field strains the material. As a consequence, electromagnetic phenomena couples to the mechanical phenomena.

We first start with the link between electromagnetics and acoustics, the polarization vector **P**:

$$\mathbf{P} = N\mathbf{p} = \epsilon_0 \kappa \mathbf{E}, \tag{2.61}$$

where N is the number of dipoles per unit volume, **p** corresponds to the dipole moment per unit volume, and κ relates the polarization vector to the electric field, where $\epsilon = \epsilon_0(1 + \kappa)$. Exposing a material to an electric field can *polarize* the material, where ions separate into positive and negative regions. In a piezoelectric material, stresses can reorient dipole moments, affecting the net polarization. The relationship between stress and polarization is the piezoelectric matrix, d ($\mathrm{C{\cdot}N^{-1}}$):

$$P_i = d_{ijk} T_{jk} \implies \mathbf{P} = \mathbf{d} : \mathbf{T} \implies \mathbf{D} = \epsilon \mathbf{E}, \tag{2.62}$$

after substituting $\epsilon = \epsilon_0(1 + \kappa)$. The electrical displacement is related to strain by the piezoelectric constant matrix, e:

$$\mathbf{D} = \mathbf{e}\mathbf{S}. \tag{2.63}$$

Moreover, the stress can be related to the electric field by means of the piezoelectric constant matrix, e:

$$T_i = -e_{ik} E_k. \tag{2.64}$$

Ignoring losses due to crystal viscosity, the following two equations are known as the piezoelectric constitutive equations, obtained by adding electrical terms to (2.2) and

(2.13):

$$\mathbf{T} = \mathbf{c}^E \cdot \mathbf{S} - \mathbf{e} : \mathbf{E}, \tag{2.65}$$

$$\mathbf{D} = \epsilon^S \cdot \mathbf{E} + \mathbf{e} : \mathbf{S}, \tag{2.66}$$

where the elastic and permittivity tensors are taken at constant electric field (grounded) and constant strain (no mechanical force), respectively, because the coupling of mechanical and electrical phenomena could alter the material constants.

Due to the vector-nature of the polarization vector, materials with a center of symmetry cannot be piezoelectric. To see why, consider a crystal possessing a center of symmetry, being acted on by a polarization. This polarization induces a strain in the material. Flipping it through the center of symmetry, the strain remains the same whereas the polarization vector changes direction. This can only happen if the polarization vector is zero.

2.6 Plane Waves in Piezoelectric Solids

We now have concise constitutive equations for relating acoustic and electromagnetic phenomena in materials. What is left is to find a wave equation in piezoelectric media. We start with the electromagnetic field equations, assuming the medium is lossless, no applied forces, and there is no source current:

$$-\nabla \times \mathbf{E} = \frac{\partial \mathbf{B}}{\partial t}, \tag{2.67}$$

$$\nabla \times \mathbf{H} = \frac{\partial \mathbf{D}}{\partial t}, \tag{2.68}$$

as well as the acoustic field equations:

$$\nabla \cdot \mathbf{T} = \frac{\partial \mathbf{p}}{\partial t}, \tag{2.69}$$

$$\nabla_s \mathbf{v} = \frac{\partial \mathbf{S}}{\partial t}, \tag{2.70}$$

Electromagnetic equations have two plane wave solutions, whereas acoustic equations have three. In piezoelectric media, these are coupled together through the constitutive equations. Thus, solutions to a wave equation are electromagnetic-acoustic waves of which there should be five. Assume that materials are nonmagnetic:

$$\mathbf{B} = \mu_0 \mathbf{H}, \tag{2.71}$$

implying the two fields are parallel to each other.

To produce a wave equation, we first eliminate unnecessary variables. Start with eliminating **T** and **H** from the acoustic and electromagnetic field equations, respectively. Multiplying (2.70) by c^E yields:

$$\mathbf{c}^E : \nabla_s \mathbf{v} = \mathbf{c}^E : \frac{\partial \mathbf{S}}{\partial t}. \tag{2.72}$$

Taking the time derivative of (2.65), and assuming the stress constants are invariant with time, obtains:

$$\frac{\partial \mathbf{T}}{\partial t} = \mathbf{c}^E : \frac{\partial \mathbf{S}}{\partial t} - \mathbf{e} \cdot \frac{\partial \mathbf{E}}{\partial t}. \tag{2.73}$$

Substituting (2.70) into (2.73):

$$\frac{\partial \mathbf{T}}{\partial t} = \mathbf{c}^E : \nabla_s \mathbf{v} - \mathbf{e} \cdot \frac{\partial \mathbf{E}}{\partial t}. \tag{2.74}$$

Taking the time derivative of (2.69) yields:

$$\nabla \cdot \left(\frac{\partial \mathbf{T}}{\partial t} \right) = \rho \frac{\partial^2 \mathbf{v}}{\partial t^2}. \tag{2.75}$$

Inserting (2.74) into (2.75) and rearranging obtains:

$$\nabla \cdot \mathbf{c}^E : \nabla_s \mathbf{v} = \rho \frac{\partial^2 \mathbf{v}}{\partial t^2} + \nabla \cdot \left(\mathbf{e} \cdot \frac{\partial \mathbf{E}}{\partial t} \right). \tag{2.76}$$

We can take the curl of (2.67) and substitute (2.71) to yield:

$$-\nabla \times \nabla \times \mathbf{E} = \mu_0 \frac{\partial}{\partial t} \nabla \times \mathbf{H}. \tag{2.77}$$

Taking the time derivative of (2.68) yields:

$$\frac{\partial}{\partial t} (\nabla \times \mathbf{H}) = \frac{\partial^2 \mathbf{D}}{\partial t^2}. \tag{2.78}$$

Due to (2.78), (2.77) becomes:

$$-\nabla \times \nabla \times \mathbf{E} = \mu_0 \left(\frac{\partial^2 \mathbf{D}}{\partial t^2} \right). \tag{2.79}$$

The second temporal derivative of (2.66) is:

$$\frac{\partial^2 \mathbf{D}}{\partial t^2} = \epsilon^S \cdot \frac{\partial^2 \mathbf{E}}{\partial t^2} + e : \nabla_s \frac{\partial \mathbf{v}}{\partial t}. \tag{2.80}$$

Substituting (2.80) into (2.79) yields:

$$-\nabla \times \nabla \times \mathbf{E} = \mu_0 \left(\epsilon^S \cdot \frac{\partial^2 \mathbf{E}}{\partial t^2} + \mathbf{e} : \nabla_s \frac{\partial \mathbf{v}}{\partial t} \right). \tag{2.81}$$

Equation (2.81) is the Christoffel equation coupled with an electrical perturbation.

We can express these formulas in terms of matrix components and matrix-differential operators, where

$$\nabla \cdot \mathbf{c}^E : \nabla_s \mathbf{v} \implies \Gamma_{ij}, \tag{2.82}$$

$$\nabla \cdot \left(\mathbf{e} \cdot \frac{\partial \mathbf{E}}{\partial t} \right) \implies \nabla_{iK} e_{Kl} \frac{\partial E_l}{\partial t} \implies -jkl_{iK} e_{Kl} \frac{\partial E_l}{\partial t}, \tag{2.83}$$

$$\mu_0 \mathbf{e} : \nabla_s \frac{\partial \mathbf{v}}{\partial t} \implies \mu_0 e_{iI} \nabla_{Ij} v_j \implies -\mu_0 e_{iI} jkl_{Ij} v_j. \tag{2.84}$$

2.7 Quasistatic Approximation

For waves with multiple direction particle displacements, the curl of **E** cannot be zero. When the wave has one particle displacement, the coupled electric field does not rotate

and is called a quasistatic electric field. In this case, the electric field has a zero curl (despite varying with time), and hence can be written as the gradient of a potential function, ϕ

$$\mathbf{E} = -\nabla\phi. \tag{2.85}$$

As a consequence, there is no acoustically generated magnetic field. Furthermore, the size of the electroacoustic device is much smaller than the corresponding electromagnetic wavelength. Lastly, the electric field propagates at the acoustic velocity in the crystal, and the electric field is in the direction of acoustic displacement. Substituting (2.85) into (2.81), and using vector identities ($\nabla \times \nabla\phi = 0$ and $\nabla \cdot (\nabla \cdot \mathbf{E}) = 0$) yields:

$$\nabla \cdot \mathbf{c} : \nabla_s \mathbf{v} - \rho \frac{\partial^2 \mathbf{v}}{\partial t^2} = -\nabla \cdot \mathbf{e} : \frac{\partial \nabla\phi}{\partial t}. \tag{2.86}$$

Taking the divergence of (2.81) obtains:

$$0 = -\mu_0 \nabla \cdot \epsilon^S : \frac{\partial^2 \nabla\phi}{\partial t^2} + \mu_0 \nabla \cdot \left(\mathbf{e} : \nabla_S \frac{\partial \mathbf{v}}{\partial t} \right). \tag{2.87}$$

Converting to plane-wave formalism yields:

$$-k^2 (l_{iJ} c_{JI} l_{Ij}) v_j + \rho\omega^2 v_i = j\omega k^2 (l_{iJ} e_{Jj} l_j)\phi. \tag{2.88}$$

Then, noting that $\nabla\phi = -jkl_j\phi$, we have:

$$0 = \omega^2 k^2 (l_i \epsilon^S_{ij} l_j)\phi - j\omega k^2 (l_i e_{iL} l_{Lj}) v_j. \tag{2.89}$$

Solving (2.89) for the potential:

$$\phi = \frac{1}{j\omega} \left(\frac{(l_i e_{iL} l_{Lj}) v_j}{l_i \epsilon^S_{ij} l_j} \right). \tag{2.90}$$

Substituting (2.90) into (2.88) yields:

$$k^2 \left(l_{iJ} \left(c_{JI}^E + \frac{(e_{Kj}l_j)(l_i e_{iL})}{l_i \epsilon_{ij}^S l_j} \right) l_{Ij} \right) v_j = \rho \omega^2 v_i. \tag{2.91}$$

Equation (2.91) is called the stiffened Christoffel equation. It is a three-dimensional piezoelectric wave equation.

2.8 Wave Analysis

As stated previously, there are three acoustic modes in crystals which appear as elastic standing waves: Two shear modes and one longitudinal mode. The thickness shear mode propagates through the thickness of the crystal with a velocity:

$$v_s = f\lambda, \tag{2.92}$$

where f denotes the frequency of the wave and λ is the wavelength. The properties of the crystal, including its density, material tensors and orientation determine the velocity. The particle displacement will be subject to geometry as follows:

$$h = \frac{n\lambda}{2}, \tag{2.93}$$

where n is a natural number whose value is based on the method of excitation. In thickness field excitation, the waves must be subject to electrical boundary conditions; that is, there must be voltages of opposite polarity on either side (Pinkham, 2007) due to the presence of metal on both sides. Thus, n can only take on odd values. For lateral field excitation, even harmonics can be excited, so n can be even. Below is pictured the first few harmonics, with arrows denoting the direction of displacement:

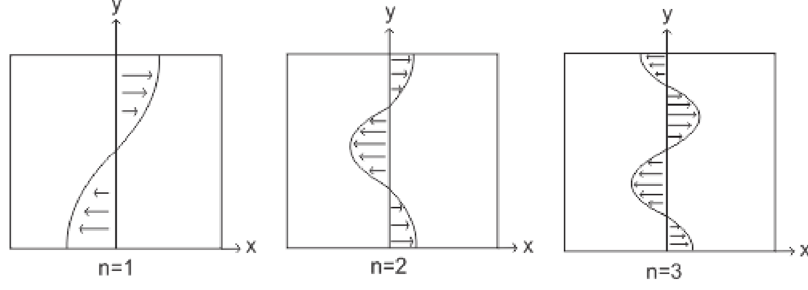

Figure 7: First Three Harmonics

Solving (2.93) for λ and inserting into (2.92) yields:

$$f_n = \frac{nv_s}{2h}, \tag{2.94}$$

where f_n denotes the nth harmonic of this acoustic mode. Thus, the fundamental resonant frequency of a 1μm thick AlN device is 3.06 GHz.

2.9 Symmetry Considerations

AlN grows most easily as a hexagonal wurtzite crystal, which has 6-fold rotation symmetry. As a consequence, the symmetry axis is c, with three secondary axes in the basal plane labeled a_1, a_2, and a_3. The following derivations of the material tensors for a hexagonal crystal follow the procedures outlined by Nye (1959), where the details are filled in explicitly. The idea is to rotate the axes and find relationships between the tensor constants before and after transformation, using the symmetry properties of the crystal. We start with the second-order permittivity tensor.

To find the components of the permittivity tensor, we use the rotation matrix of $60°$ parallel to the x_3 axis:

$$R(\theta) = \begin{bmatrix} \frac{1}{2} & \frac{1}{2}\sqrt{3} & 0 \\ -\frac{1}{2}\sqrt{3} & \frac{1}{2} & 0 \\ 0 & 0 & 1 \end{bmatrix}. \tag{2.95}$$

The second-order tensor transformation equation is:

$$\epsilon'_{ij} = \frac{\partial x'_i}{\partial x_k}\frac{\partial x'_j}{\partial x_l}\epsilon_{kl}. \tag{2.96}$$

It can be shown that the second-order permittivity tensor is symmetric. Therefore, $\epsilon_{ij} = \epsilon_{ji}$. Using equation (2.96), we find a set of equations relating the components before and after transformation:

$$\epsilon'_{11} = \frac{1}{4}\epsilon_{11} + \frac{\sqrt{3}}{2}\epsilon_{12} + \frac{3}{4}\epsilon_{22}, \tag{2.97}$$

$$\epsilon'_{12} = -\frac{\sqrt{3}}{4}\epsilon_{11} - \frac{1}{2}\epsilon_{12} + \frac{\sqrt{3}}{4}\epsilon_{22}, \tag{2.98}$$

$$\epsilon'_{22} = \frac{3}{4}\epsilon_{11} + \frac{\sqrt{3}}{2}\epsilon_{12} + \frac{1}{4}\epsilon_{22}, \tag{2.99}$$

$$\epsilon'_{13} = \frac{1}{2}\epsilon_{13} - \frac{\sqrt{3}}{2}\epsilon_{23}, \tag{2.100}$$

$$\epsilon'_{23} = \frac{\sqrt{3}}{2}\epsilon_{13} + \frac{1}{2}\epsilon_{23}, \tag{2.101}$$

$$\epsilon'_{33} = \epsilon_{33}. \tag{2.102}$$

Due to the symmetry of the crystal, $\epsilon'_{13} = \epsilon_{13}$, and $\epsilon'_{23} = \epsilon_{23}$. Therefore, these terms must be zero. All of the other terms drop out due to symmetry. Equations (2.97-99) can be solved simultaneously yielding:

$$\epsilon_{11} = \epsilon_{22}. \tag{2.103}$$

Hence the permittivity tensor is:

$$\begin{bmatrix} \epsilon_1 & 0 & 0 \\ 0 & \epsilon_1 & 0 \\ 0 & 0 & \epsilon_3 \end{bmatrix}, \tag{2.104}$$

where the subscripts have been shortened.

For the piezoelectric tensors, the terms leftover are:

$$\begin{bmatrix} 0 & 0 & 0 & 0 & d_{15} & 0 \\ 0 & 0 & 0 & d_{15} & 0 & 0 \\ d_{31} & d_{31} & d_{33} & 0 & 0 & 0 \end{bmatrix} \begin{bmatrix} 0 & 0 & 0 & 0 & e_{15} & 0 \\ 0 & 0 & 0 & e_{15} & 0 & 0 \\ e_{31} & e_{31} & e_{33} & 0 & 0 & 0 \end{bmatrix}, \tag{2.105}$$

and for the elastic tensor, calculations reveal:

$$c^E = \begin{bmatrix} c_{11} & c_{12} & c_{13} & 0 & 0 & 0 \\ c_{12} & c_{11} & c_{13} & 0 & 0 & 0 \\ c_{13} & c_{13} & c_{33} & 0 & 0 & 0 \\ 0 & 0 & 0 & c_{44} & 0 & 0 \\ 0 & 0 & 0 & 0 & c_{44} & 0 \\ 0 & 0 & 0 & 0 & 0 & c_{66} \end{bmatrix}, \tag{2.106}$$

where $c_{66} = \frac{c_{11}-c_{12}}{2}$.

Applying the piezoelectrically stiffened Christoffel equation to a crystal with hexagonal symmetry (Corso, Dickherber, & Hunt, 2007) and the material constants of aluminum nitride provides a starting point for the analysis of this device:

$$k^2 \left(l_{iJ} \left(c_{JI}^E + \frac{(e_{Kj} l_j)(l_i e_{iL})}{l_i \epsilon_{ij}^S l_j} \right) l_{Ij} \right) v_j = \rho \omega^2 v_i. \tag{2.107}$$

Under the assumption of lateral field excitation, the electric-field remains in the $x - y$ plane. Consequently, $l_z = 0$ and $l_x^2 + l_y^2 = 1$ due to normalization. Using the aforementioned matrices for a hexagonal symmetry, the Christoffel matrix for hexagonal AlN takes the form:

$$\Gamma = \begin{bmatrix} c_{44} + \frac{e_{15}^2 l_x^2}{\epsilon_{11}} & \frac{e_{15}^2 l_x l_y}{\epsilon_{11}} & 0 \\ \frac{e_{15}^2 l_x l_y}{\epsilon_{11}} & c_{44} + \frac{e_{15}^2 l_y^2}{\epsilon_{11}} & 0 \\ 0 & 0 & c_{33}. \end{bmatrix} \tag{2.108}$$

This equation can be solved for particle displacement (eigenvectors) and velocities

(eigenvalues). The eigenvectors and their associated eigenvalues are:

$$u_1 = \begin{bmatrix} -E_y \\ E_x \\ 0 \end{bmatrix} \quad v_1 = c_{44}, \tag{2.109}$$

$$u_2 = \begin{bmatrix} E_x \\ E_y \\ 0 \end{bmatrix} \quad v_2 = c_{44} + \frac{e_{15}^2}{\epsilon_{11}}, \tag{2.110}$$

$$u_3 = \begin{bmatrix} 0 \\ 0 \\ 0 \end{bmatrix} \quad v_2 = c_{33}. \tag{2.111}$$

As we can see, only the shear mode (2.110) is piezoelectrically excited, due to the electrical term added to the velocity. Furthermore, the particle displacement is in the same direction as the electric field, indicating that lateral field excitation produces a pure shear mode.

2.10 Finite Element Modeling

Finite element modeling is a numerical analysis technique used to solve partial differential equations, which are often coupled together and have initial or boundary conditions. The basic principle includes partitioning a continuous geometry into discrete nodes, and solving the equation at each node. The solution to the continuous problem will be approximated by the connection of all of the nodes. The software package is COMSOL multiphysics. This software enabled the investigation of the electric field vectors, electrical energy density, and simulations of the admittance and Q for LFE devices. In all cases, the microelectro-mechanical systems (MEMS) module was used.

To start, the geometry must be defined. This consisted of four subdomains of silicon (isotropic), aluminum nitride, and two aluminum electrodes (both anisotropic and directly on top of the aluminum nitride for lateral field excitation). The aluminum nitride

was piezoelectric and all other subdomains were decoupled. The boundary conditions applied were: One electrode at +1V potential, one electrode grounded, and every other electrical boundary was either zero charge or symmetry. Mechanical boundary conditions were also used to ensure that the ends of the device remained fixed. Perfectly matched layers were formed following Zampolli, Malm, and Tesei (2008), using an absorption coefficient in the x-direction, to encourage wave attenuation at the ends of the resonator to avoid spurious reflections. The meshing was between coarse and fine (as extremely fine meshes require intense computing power). The electric field lines (using streamlines) and electrical energy density were as follows:

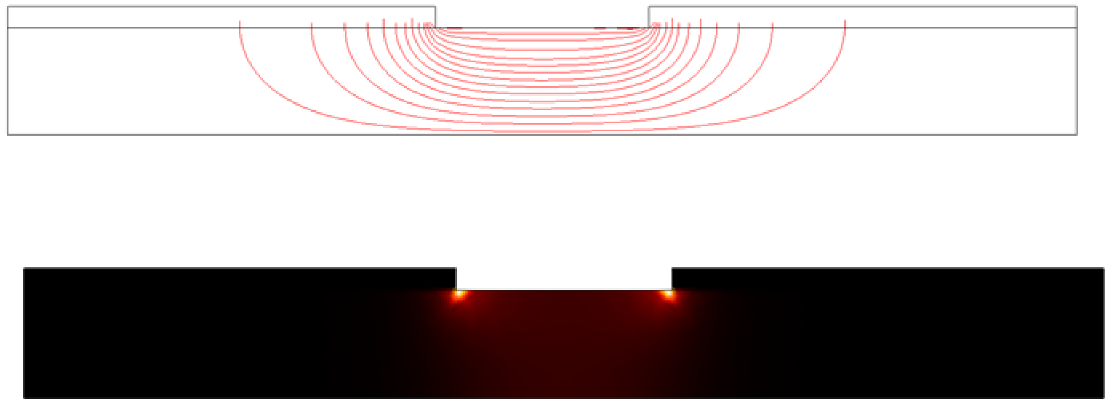

Figure 8: Electric Field Lines and Energy Density

This figure confirms that the fringe fields emanating from the electrode at a positive potential possess a strong horizontal component in the active area of the sensor. In addition, the electrical energy density is at a maximum where the sensor is exposed to the measurand. Moreover, a frequency response analysis was conducted, mostly following ("Thin Film BAW Resonator", n.d.), where the admittance, imaginary part of the admittance, and mechanical quality factor were calculated using predefined COMSOL variables. The admittance was calculated using the current running through the +1V electrode:

$$Y = \frac{J_{ns}}{V_0}, \tag{2.112}$$

where Y is the admittance, J_{ns} is the current through the electrode, and V_0 is the applied voltage. The quality factor was obtained from the edges of the perfectly matched layers, where:

$$Q = \frac{\omega W_{tot}}{Q_{tot}}, \tag{2.113}$$

where Q is the quality factor, ω is the angular frequency, W_{tot} is the peak stored energy, and Q_{tot} is the time average power dissipation. Structural (.001) and dielectric loss factors (.0005) were also included ("Aluminum Nitride," 2007). The admittance, imaginary part of the admittance, and quality factor are plotted below versus frequency:

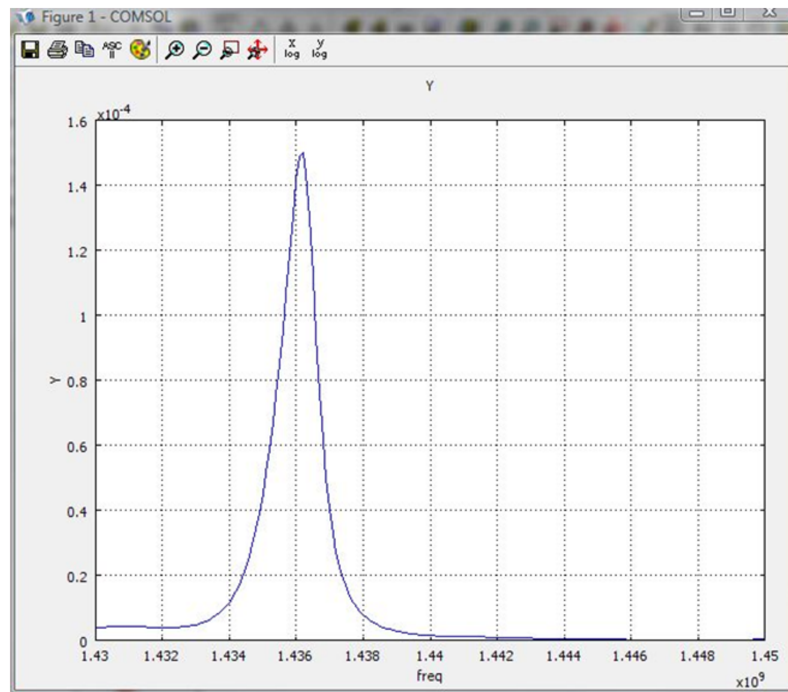

Figure 9: COMSOL Magnitude of the Admittance

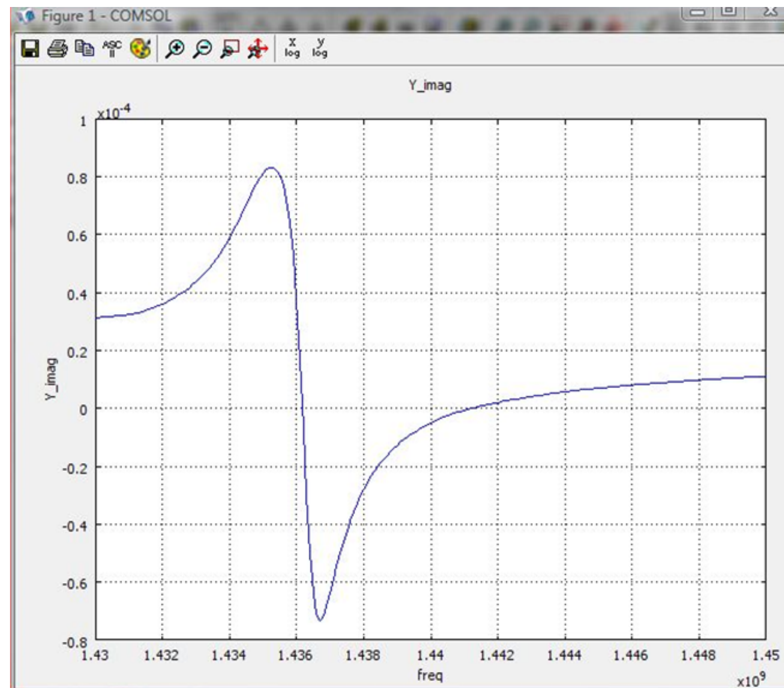

Figure 10: Imaginary Part of the Admittance

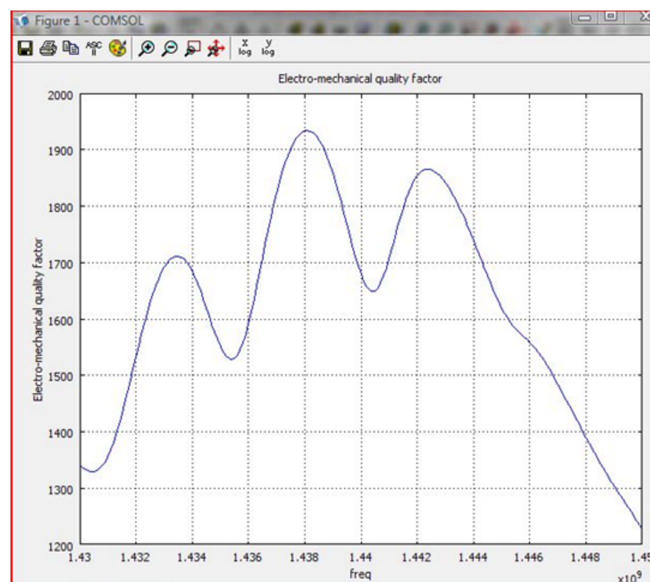

Figure 11: Quality Factor

A 2μm device resonates at about 1.58 GHz, which is around .15GHz off from the predicted frequency. The inclusion of loss factors could have decreased the frequency. As a consequence, it seems reasonable to say that COMSOL predicts some sort of

resonance in that structure.

3 Materials and Methods

3.1 AlN

Recently, FBAR devices have been realized using AlN, ZnO, InN, and GaN compounds. AlN has received much attention in recent years due to its hardness (7 on Moh's hardness scale) ("Properties of Typical Aluminum Nitride Substrates," n.d.), high bulk acoustic velocity (approximately 6333 m/s for the transverse shear mode and 10172 m/s for the longitudinal mode) (Chen, Wang, D. Li, Xu, & Z. Li, 2011), moderate piezoelectric coupling coefficient (3.1-8%) (Fu et al., 2010) low dielectric losses due to its wide bandgap of 6.2eV (Dubois & Muralt, 1999), and chemical stability. These qualities emphasize the suitability of AlN for piezoelectric applications.

AlN typically grows in the wurtzite structure consisting of columnar grains. For liquid-phase sensing, obtaining pure c-axis AlN is of high importance, since lateral fields will purely excite the shear mode. The shear mode is optimal because liquids cannot support it due to a lack of rigidity, so no energy would be leaked out due to compressional motion. The growth of c-axis AlN has been carried out using a number of methods, including RF magnetron sputtering, molecular beam epitaxy (MBE), and e-beam evaporation. Hexagonal AlN has point-group and space-group symmetries of 6mm and $P6_3mc$, respectively (Mokoc, 1999). AlN can also grow in the cubic structure, typically with increased sputtering pressures, but fabrication methods for cubic AlN suffer from irreproducibility and difficulty (Zhu, Zhao, Luo, Zhang, & Li, 2008).

3.2 AlN Material Constants

The constants of AlN, which determine some physical properties such as piezoelectric coupling, will be discussed. The elastic stiffness tensor for AlN is ($\times 10^9$ N·m^{-2}):

$$c^E = \begin{bmatrix} 345 & 125 & 120 & 0 & 0 & 0 \\ 125 & 345 & 120 & 0 & 0 & 0 \\ 120 & 120 & 395 & 0 & 0 & 0 \\ 0 & 0 & 0 & 118 & 0 & 0 \\ 0 & 0 & 0 & 0 & 118 & 0 \\ 0 & 0 & 0 & 0 & 0 & 110 \end{bmatrix}, \tag{3.1}$$

where c_E denotes the stiffness at a constant electric field. The piezoelectric stress matrix reflects the relationship between an applied electric field and the resulting stress in a piezoelectric crystal (in C·m^{-2}):

$$e = \begin{bmatrix} 0 & 0 & 0 & 0 & -0.48 & 0 \\ 0 & 0 & 0 & -0.48 & 0 & 0 \\ -0.58 & -0.58 & 1.55 & 0 & 0 & 0 \end{bmatrix}. \tag{3.2}$$

Finally, the permittivity matrix represents the amount of electric flux that charges create at constant strain ($\times 10^{-11}$ F·m^{-1}):

$$\epsilon^S = \begin{bmatrix} 8.0 & 0 & 0 \\ 0 & 8.0 & 0 \\ 0 & 0 & 9.5 \end{bmatrix}. \tag{3.3}$$

3.3 Butterworth Van-Dyke Equivalent Circuit

For FBARs, a modified Butterworth Van-Dyke model was developed by Larson, Bradley, Wartenberg, and Ruby (2000), which models the operation of the resonator, seen in Fig. 12:

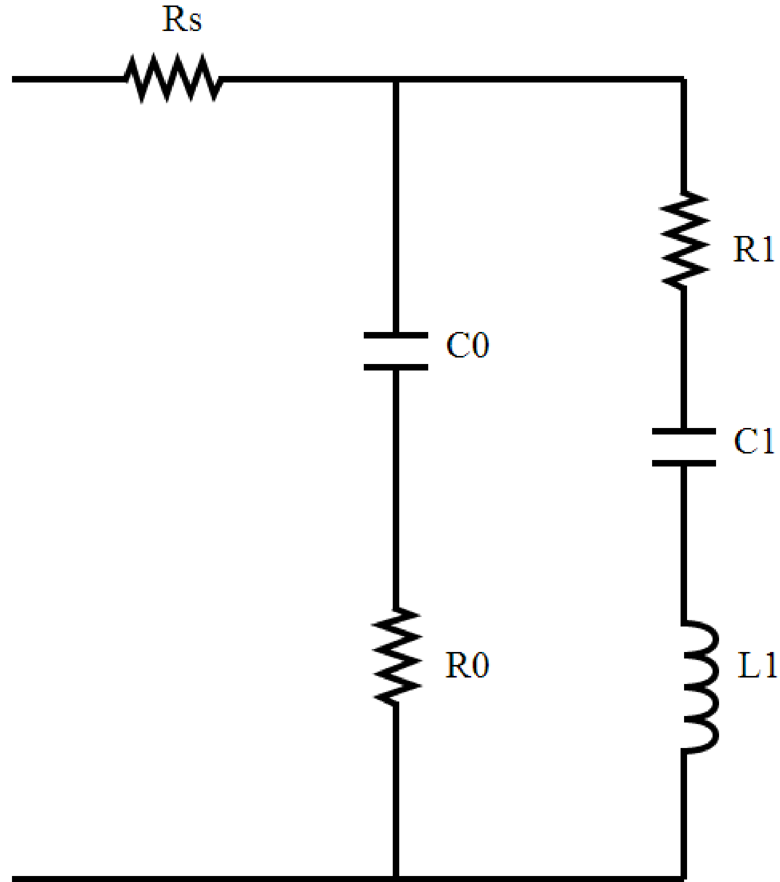

Figure 12: Modified Butterworth Van-Dyke Circuit

Each element corresponds to a physical entity. The right side branch, called the motional arm, includes three elements in series, where R_1, L_1, and C_1 represent the motional resistance, motional inductance, and motional capacitance, respectively. Physically, the motional resistance deals with the viscosity or energy dissipation in the film, the motional inductance relates to the inertia, and the motional capacitance represents the elasticity or energy stored in the film (Vetelino & Reghu, 2010). Conversely, the left side (static branch) consists of a capacitor C_o and resistor R_o in series. C_o corresponds to the capacitance between the electrodes (called the clamped capacitance), whereas R_o describes dielectric losses manifesting itself as electrode resistance. R_s denotes any parasitic resistance encountered. Clearly, the motional arm deals with the electro-acoustical properties of the film. An oscillating piezoelectric crystal experiences

resonance when the conversion between electrical and mechanical energy reaches its highest. For series resonance, the impedance takes on a minimum value. In the case of parallel resonance, the impedance assumes a maximum value. Furthermore, at resonance L_1 has the same impedance as C_1 but is phase-shifted by 90 degrees, leaving the series portion R_1. A phase graph can indicate whether phase-shifting occurred. A Smith Chart also allows one to observe resonance, where a signal would appear as circular (oscillating between inductance and capacitance) during this phenomenon.

Using computer software, the parameters of a resonator (which are based on physical and material characteristics of the device) can be extracted and used to predict the electromechanical coupling coefficient and the Q. The impedance can be calculated using a simple loop, where Z_1 refers to the impedance of the motional arm, Z_2 corresponds to the impedance with the clamped capacitance and parasitic resistance, and Y_{eq} is the equivalent admittance of the resonator:

$$Z_1 = R_1 + j\omega L_1 + \frac{1}{j\omega C_1}, \tag{3.4}$$

$$Z_2 = R_s + \frac{1}{j\omega C_0} + Z_1, \tag{3.5}$$

$$Y_{eq} = \frac{1}{Z_2}. \tag{3.6}$$

A loop can be created for 20,001 data points using guess values for the physical parameters. The guess values are reevaluted if the plot does not match the data, and the process is reiterated until a qualitative match is achieved.

3.4 Quality Factor

The concept of quality has been mentioned previously, but an in-depth discussion is warranted due to the influence of quality factors on sensor performance. The quality of a resonator can be degraded due to a number of damping factors, such as air and support, surface effects, and thermoelastic damping. At resonance frequency, f, the maximum energy is stored in the resonator. However, losses spread the oscillation

energy on a bandwidth B about the resonant frequency, implying the quality factor can be described as:

$$Q = \frac{f}{B},$$

where B is defined between -3 dB frequencies about f (Campanella, 2010). Quality can also be expressed in terms of material constants, by relating the parameters of the material to electrical characteristics of the resonator (such as impedance) (Rosenbaum, 1988).

3.5 Chemical Bond of AlN

Chemically, aluminum and nitrogen atoms can form two different bonds in the wurtzite structure, differing by which axis they bond along (a or c). In total, three bonds occur along the a-axis and one bond forms along the c-axis. Fig. 13 conveys this structure (Xu, Zhang, & Jin, 2001):

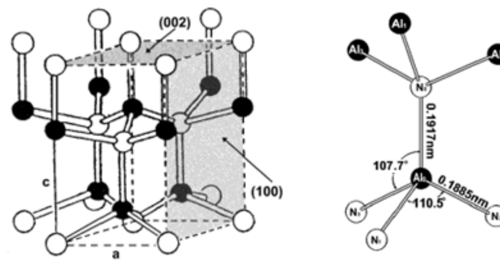

Figure 13: Bonds of Aluminum Nitride

As one can see, “distorted” tetrahedrons form. The two different bonds have lengths of 0.1885 and 0.1917 nm for the a- and c- axes respectively, with the lattice constants being a = 0:3110 nm and c = 0:4980 nm (Xu et al., 2001). For certain bonds, sp3-hybridization occurs, which basically means the s and p orbitals create hybrid orbitals to increase the number of bonds allowed. Since the outer orbitals of aluminum are the most reactive, the 3s and 3p orbitals mesh together to form four sp3 orbitals. Likewise, the 2s and 2p orbitals for nitrogen also combine. The aluminum atom has three semi-full orbits and one full orbit, whereas nitrogen possesses three semi-full orbits and

one full orbit. Coupling the semi-full orbits together results in bonds along the a-axis, whereas the other bond (full and empty orbits) occurs along the c-axis. This c-axis bond, characterized by being more ionic, has a lower bonding energy. Hence this bond easily breaks due to applied energy, indicating that there are energy considerations for fabricating AlN.

3.6 RF Magnetron Sputtering

To produce uniform thin films of various compounds, one can use a host of different techniques, such as chemical vapor deposition (CVD), e-beam evaporation, molecular beam epitaxy (MBE), or magnetron sputtering. For AlN, reactive magnetron sputtering presents a number of advantages. First, the substrate temperature required maintains lower values than other processes (CVD, MBE), allowing for CMOS applications. Since diffusion exponentially depends on temperature, CMOS structures can be disrupted because of thermal expansion. Furthermore, power supplies can be split between multiple targets (confocal configuration), allowing for more efficient depositions along with the possibility of using multiple metals. In addition, the substrate remains motionless other than rotation. Compared to diode sputtering, the magnetron offers two key advantages. First, an increased path length for the electrons provides a higher probability for the ionization of the argon atoms. Secondly, the magnetron confines the plasma, preventing electrons from bombarding the substrate. Fig. 14 shows a basic setup of a magnetron sputtering chamber:

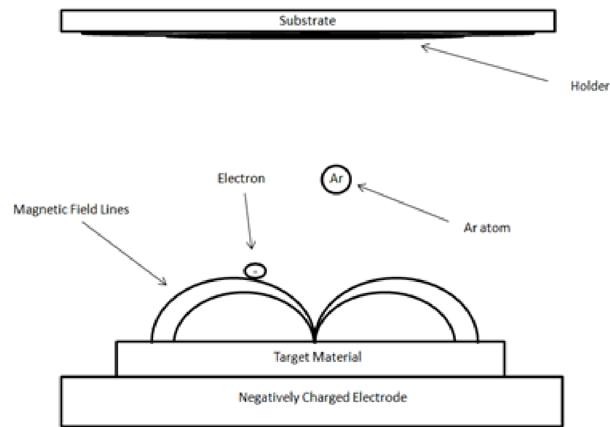

Figure 14: Magnetron Sputtering

Reactive magnetron sputtering is a physical deposition technique used to create thin films. Metal targets are placed inside a vacuum chamber, which is pumped down to an ultra-high vacuum pressure (around $\times 10^{-7}$ Torr). At a high pressure (20 mTorr), relative to the sputtering pressure, argon gas is introduced to create a plasma. This plasma consists of ions, electrons, and photons. Igniting the plasma is an electrical bias, which is powered thereafter by a RF, DC, or pulsed DC power supply. Free electrons, which are confined by the Lorentz force stemming from a magnetron, become restricted to a circular path. These electrons ionize argon, which become attracted to the anode at the bottom of the chamber. Instead of obtaining another electron, they bombard the target material and displace target atoms which float onto the substrate. This collision also releases other free electrons, which can enter the outer shells of the argon ions. Thus the argon atoms return to a neutral state and release a photon due to energy conservation, creating a glowing effect for the plasma. Nitrogen (N_2) is added to the chamber, which can nitridize the aluminum target. Moreover, nitrogen in the plasma and on the surface of the substrate can react with the aluminum atoms. The AJA-2000 at LASST uses a confocal configuration with tilted magnetrons (around 14 degrees). To increase uniformity and to avoid holder warping while heating the substrate requires turning on the rotation. An RF power supply was chosen to avoid target poisoning, as DC power would encourage charge buildup on the target.

3.6.1 Parameters

Since the growth of AlN relies on the amount of energy of the sputtered species (to an extent which orientation has an advantage affects the growth), an explanation accompanies the process parameters and their effects. To produce stoichimetric films, one can adjust the Ar/N_2 ratio. Increasing the substrate temperature affects the amount of kinetic energy given to adatoms arriving on the substrate. Inside the chamber, a quartz lamp shines an intense light onto the substrate to heat it, which is measured by a thermocouple. Sputtering pressure works in a similar manner. With a higher sputtering pressure, there are more molecules in the chamber. On the other hand, a higher flow rate increases the probability for collisions. The amount of power supplied to the argon plasma determines the initial energy of the argon atoms, and, therefore, the growth rate of the film. Choice of the power source (RF, DC, or pulsed DC) depends strongly on the target material. For an insulating target, DC suffers from charge buildup ("poisoning" by nitrogen can create an insulating layer of AlN) and can lead to arcing. Pulsed DC switches polarity to ensure charges leave the target, thereby circumventing that issue. RF presents a more costly and less efficient (shorter duty cycle) alternative to DC, but offers a power source better suited for reactions due to a higher plasma reactivity resulting from a lower growth rate (Dumiru et al., 2000). Finally, the base pressure can be somewhat altered depending on how much time one gives the chamber to pump down, any gettering (Ti being a favorable material), and a prior bake-out to absorb residual water vapor. Decreasing the base pressure reduces the amount of defects present in the film. Substrate biasing also has been used to obtain c-axis AlN films, but the ionic bombardment introduces not only a lot of stress, but argon defects in the lattice (Vergara et al., 2004). As a plus, the oxygen content becomes smaller with substrate biasing, but the argon incorporation decreases significantly the piezoelectric response.

3.7 Growth

The growth of AlN through reactive sputtering can be described by a structure zone model. This model consists of four zones: Zone 1, where shadowing effects dominate,

zones 2 and T, where surface diffusion occurs, and zone 3, in which bulk diffusion happens. The structure zone model, proposed by Thornton (1977), is pictured below:

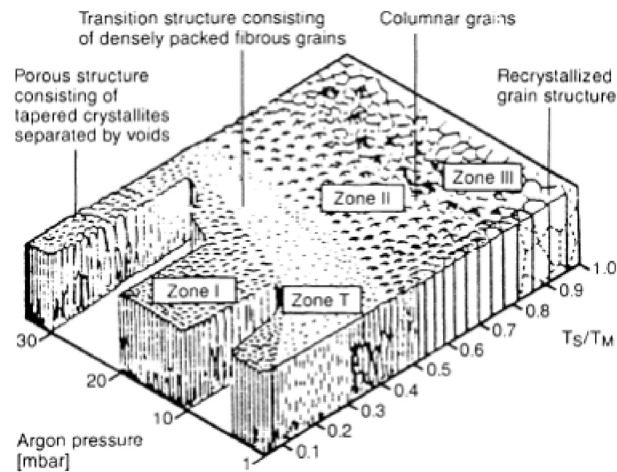

Figure 15: Structure Zone Model

AlN grows in four stages when using reactive sputter deposition. In the first stage, nucleation sites form on the substrate from arriving atoms. Secondly, these sites grow bigger as more atoms condense onto the substrate. These sites become independent islands. Eventually, they become so large that they interact with each other, where the independent islands form a collective film. However, each island has its own orientation and normal crystal plane, due to the angle of incidence and sputtering pressure. Thus, the grain distribution might not be uniform, but could be off by some angle. The orientation of the film, as a whole, is based on whichever islands have the most advantage of forming, which is based on energy considerations and growth rate.

3.8 E-beam evaporation

Another technique to grow AlN crystals is e-beam evaporation using an RF nitrogen plasma. At LASST, the e-beam system consists of a four-pocket e-gun, an RF plasma source, and a RHEED screen. The e-gun acts as an electron source. The plasma source is confined by a magnetic field and heated by a high-frequency electromagnetic field. The RHEED screen helps one ascertain the quality of the crystal being grown using

diffraction. To start, the chamber is baked and pumped down to a UHV pressure on the order of $\times 10^{-8}$ Torr. An electron beam heats up a target material, which excites the target atoms into a gaseous phase. The atoms then travel to the substrate, where they react with the nitrogen. Due to the existence of a plasma, the nitrogen becomes very mobile and the residual stress in the films is reduced. However, the substrate temperatures used to encourage epitaxial growth may be very high (on the upwards of 800°C). As a consequence, the procedure for fabricating arrays of sensors may become complicated, or an alternative method must be used.

3.9 Photolithography

Photolithography, an umbrella term for various microfabrication techniques, assists in patterning electrodes on a substrate. For the purposes of the devices mentioned in this paper, wet etching and liftoff will be discussed. Both processes focus on photoresist, a material sensitive to UV light. Two types of photoresist exist: positive and negative. A positive photoresist becomes soluble to its developer upon exposure to UV light. Conversely, for a negative photoresist, exposure to UV light renders it insoluble to its developer. To start the wet etching process includes depositioning and then spinning photoresist (S1813) on a device. Subsequent baking (105°C for three and a half minutes) allows the photoresist to harden. During the exposing stage, a low-reflective chrome mask blocks out any UV light. 2:5 NaOH:DiH2O washes away any exposed photoresist, leaving metal that can be etched. Potassium iodide etches the gold away, creating the desired pattern. Liftoff operates in a converse manner: Patterning occurs before deposition. LOR5B and 1:5 MF351:DIH2O help for the patterning portion. The exposing stage differs from etching in that UV light exposes where the desired contact shapes appear. After metal deposition, placing the devices in a bath of PG remover allows the photoresist and metals to be lifted-off. Liftoff presents a less invasive technique at the cost of more steps, but accomplishes the same result as wet etching.

3.10 Structure and X-ray Diffraction

Miller indices notate different planes in crystals. For cubic systems, three numbers represent the axes in the form (hkl). In the case of hexagonal systems, one uses four integers (called the Bravais-Miller indices). These indices include a_1, a_2, a_3, and c in the form (hkil). Each of the a-axes intersects two vertices. By way of example, Fig. 16 shows the unit cell for a hexagonal crystal:

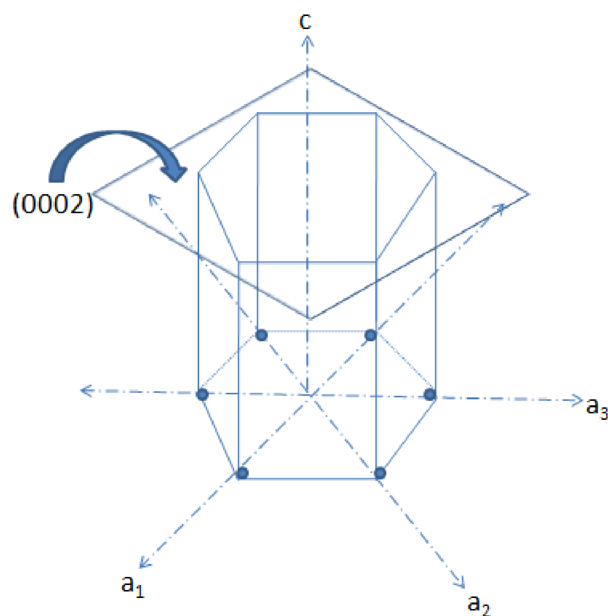

Figure 16: Hexagonal Crystal Unit Cell

For the index (0002), the plane intersects the c-axis at 2, but does not intersect any of the a-axes.

X-ray diffraction explains a technique for determing the structure of a crystal. For the purposes of this report, only $\theta - 2\theta$ scans and rocking curves will be discussed. When an x-ray beam encounters a crystal, it bounces off the atom and scatters. According to Bragg's law, for x-rays at some incident angle constructive interference will occur for the reflected beam. Some reflected angles will have a higher intensity than others, thereby indicating the arrangement of atoms in the lattice. For $\theta - 2\theta$ scans, the detector rotates around the sample with angles twice that of the incident beam. Rocking curves portray the quality of the crystal by fixing the 2θ angle and rotating about another

axis. This method shows if there is any tilt in the grains by observing the full-width at half-maximum (FWHM). A FWHM of 0 degrees would be ideal, as the film would be epitaxial.

3.11 Defects

A discussion on crystal structure warrants the mention of defects in the lattice. These defects can be vacancy generation, interstitials, or impurities. Vacancies result when an empty spot exists in the lattice where an atom would otherwise be. Interstitials occur when an atom occupies a spot where none usually exist. Finally, impurities develop when a foreign atom occupies a site that it should not. An example of an impurity would be oxygen in AlN, which occurs frequently due to the lower bonding energy between aluminum and oxygen as opposed to aluminum and nitrogen. Oxygen contamination can be a problem in magnetron sputtering if the argon purity is too low or the base pressure is too high. Since the chamber has to be opened periodically, some amount of oxygen will always be present, sometimes in water vapor. Heating the chamber before depositing, using oxygen traps or gettering the oxygen using aluminum can be ways to reduce the presence of oxygen. Microstresses can appear from defects, where a crystal experiences internal stresses as a result of these imperfections.

3.12 X-ray Photoelectron Spectroscopy

X-ray photoelectron spectroscopy (XPS) is a technique that can measure the composition of atoms in a film. Einstein's photoelectric effect underlies the principle of operation. When a thin film is bombarded with x-rays, electrons are emitted. These electrons have an energy associated with them, indicating their electron states and binding energies. Each atom has a characteristic binding energy based on different orbitals. The detector measures the binding energies, from which one can ascertain the composition of the material.

3.13 Network Analyzer

To measure properties of an electrical network, one typically uses a network analyzer. Electromagnetic waves that propagate through a transmission line can be transmitted, reflected, or absorbed. The ratio between the reflected signal to the incoming signal has an S-parameter of S_{11} or S_{22}, where S_{ij} denotes the ratio of the incoming signal (port j) to the outgoing signal (port i). Due to imperfections in a film, the reflected wave will suffer losses. A network analyzer can detail these losses through outputting the return loss (in dB). If there is no return loss, then all of the energy returned to the network analyzer. Conversely, return loss indicates that energy is being trapped in the film. During resonance, an elastic standing wave is formed in the film, in which case all of the energy is trapped in the film. Furthermore, one can measure the real and imaginary parts of admittance, as well as phase.

4 Results

The next few chapters are modified from previous REU papers that I have written along with new information.

4.1 X-ray Diffraction Results Using RF Magnetron Sputtered Films

The first two attempts were AlN on borosilicate glass with 1800W pulsed DC power split between two magnetrons, and increasing the temperature from 300° to 400°. The base pressure was around $\times 10^{-6} - \times 10^{-7}$ Torr for all sputtering attempts. The Ar/N_2 ratio stayed at 50$\%$ (altering this value proved to be unsuccessful). Sputtering pressure remained at 3mTorr for all attempts. The Al targets were at 99.999$\%$ purity. For the third and fourth attempts, the substrate was switched to fused silica. Attempt 3 the temperature was raised to 550° as well. In attempt 4, the power supply was switched to 300W RF power. A polefigure accompanies this attempt.

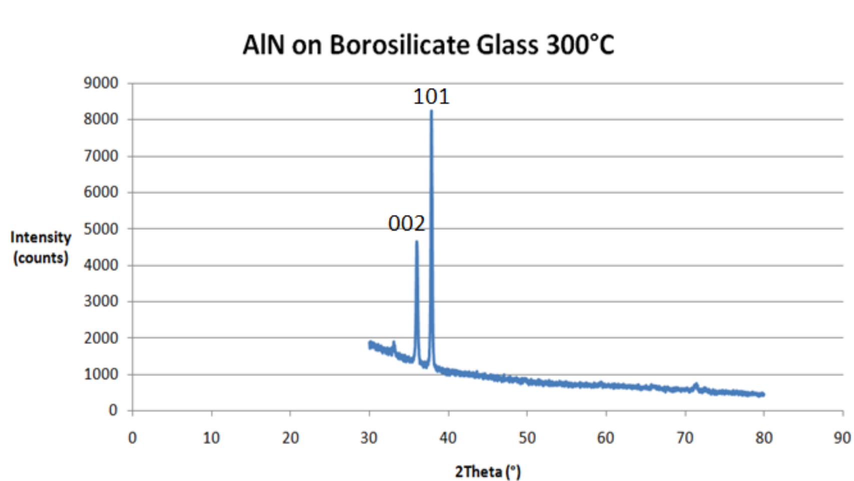

Figure 17: AlN on Borosilicate Glass at 300°C

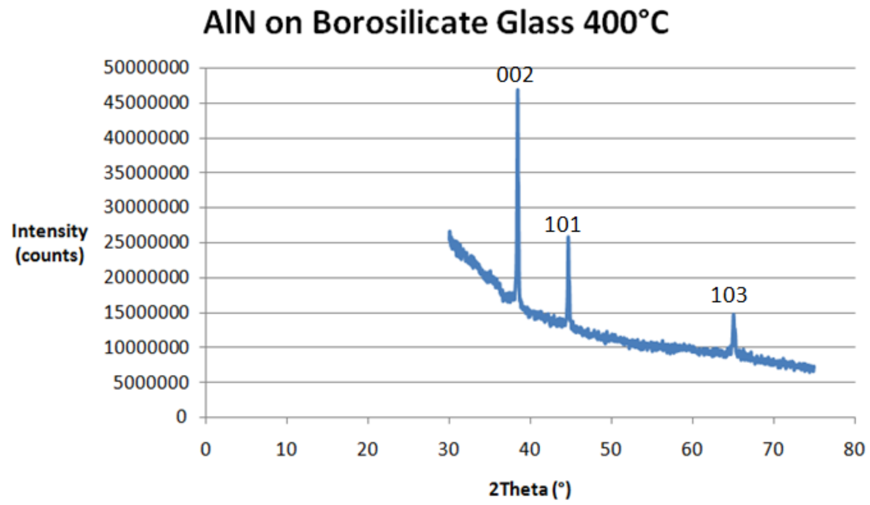

Figure 18: AlN on Borosilicate Glass at 400°C

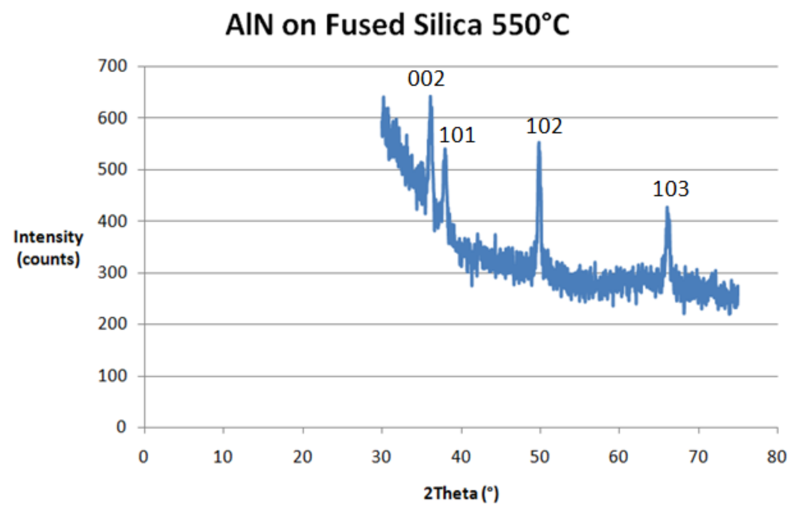

Figure 19: AlN on Fused Silica at 550°C

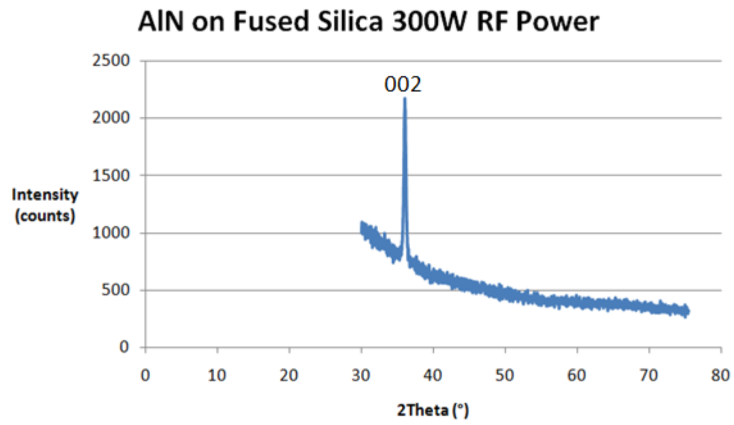

Figure 20: AlN on Fused Silica at 400°C and 300W Power

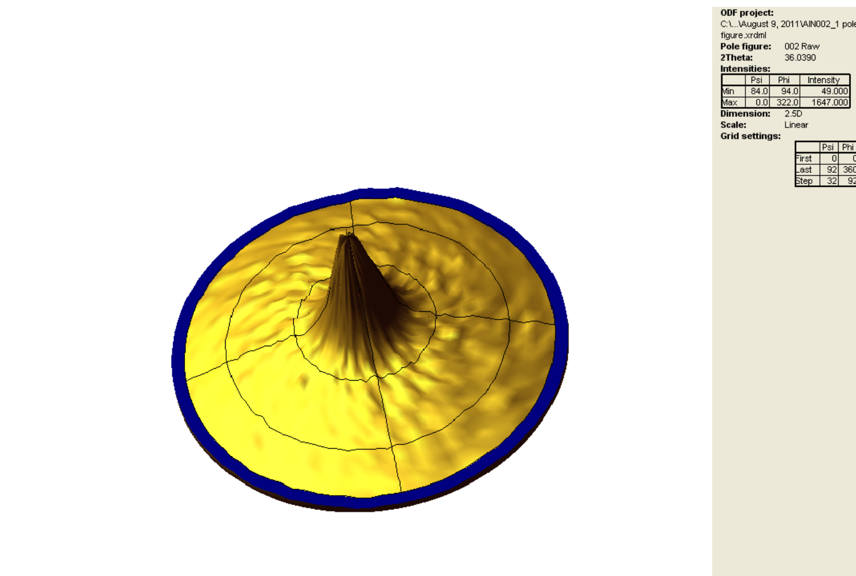

Figure 21: 002 Pole Figure

indicating that the AlN film was pure c-axis. A rocking curve of the 0002 reflection gave a FWHM of about 12°.

4.2 Network Analyzer Measurements of Magnetron Sputtered Samples

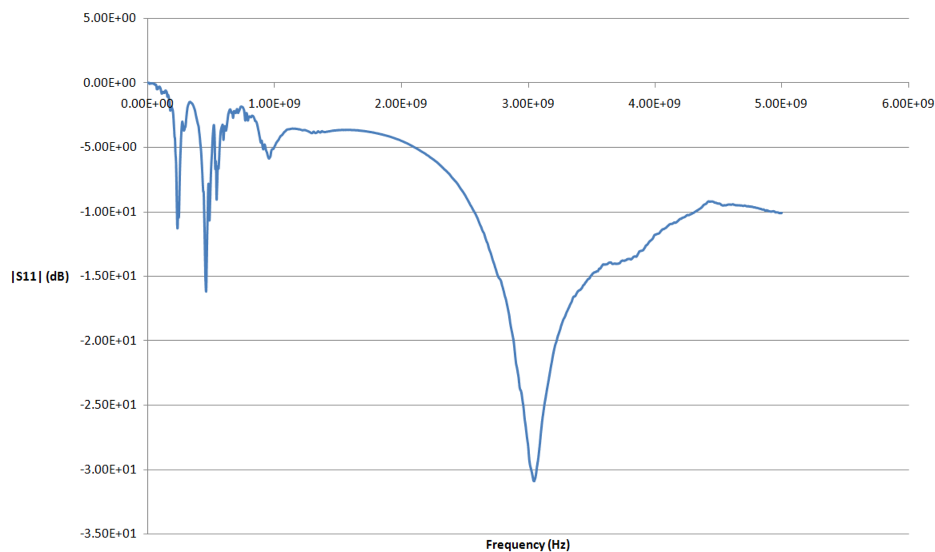

Figure 22: Return Loss of Sputtered AlN on Fused Silica

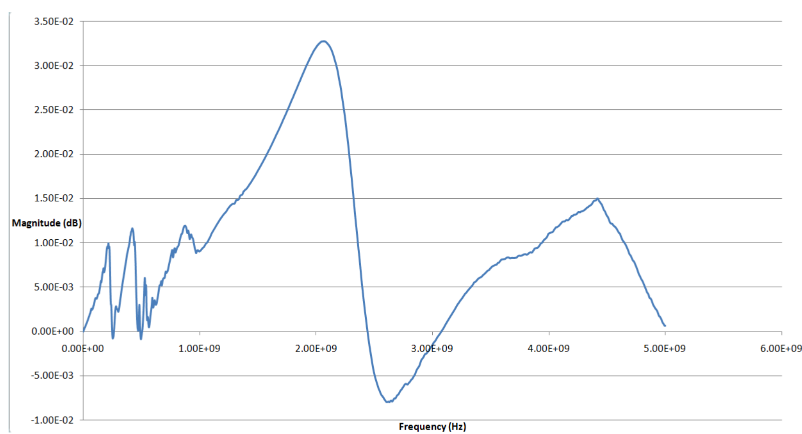

Figure 23: Susceptance of Sputtered AlN on Fused Silica

Photoresist was applied to the back of the device as an absorber, producing the following network analyzer measurement:

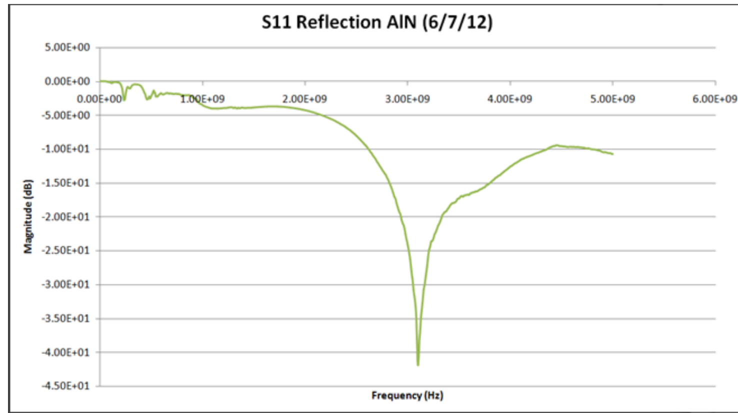

Figure 24: Return Loss of Sputtered AlN on Fused Silica after Applying Photoresist

E-beam evaporation was then used to deposit 1μm films of AlN on fused silica and c-cut sapphire with a substrate temperature of about 850°C and a deposition rate of about .1 nm/s.

4.3 E-beam Evaporation Measurements:

X-ray diffraction:

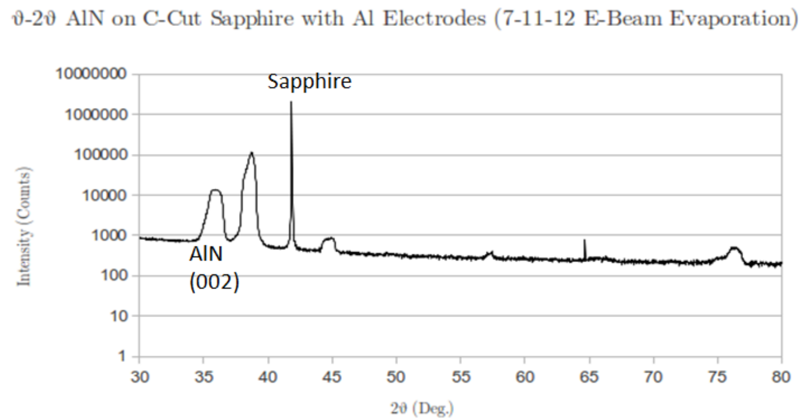

Figure 25: $\theta - 2\theta$ of AlN on Sapphire

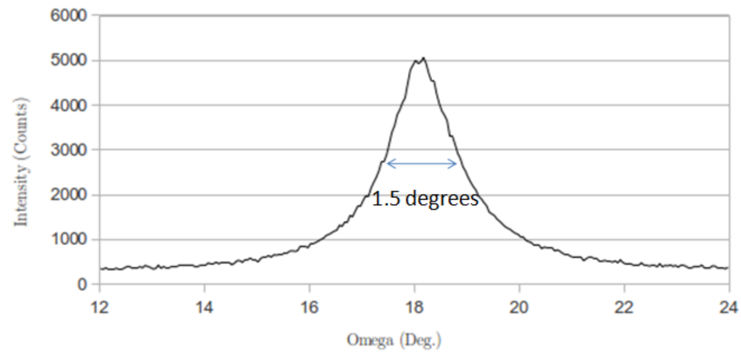

Figure 26: Full-Width at Half-Maximum of Sputtered AlN on Sapphire

X-ray photoelectron spectroscopy:

[Page 3 of 3] c:\specs data\mike f\11 july 2012 aln.vms
Date printed: 07/11/12 16:57:48

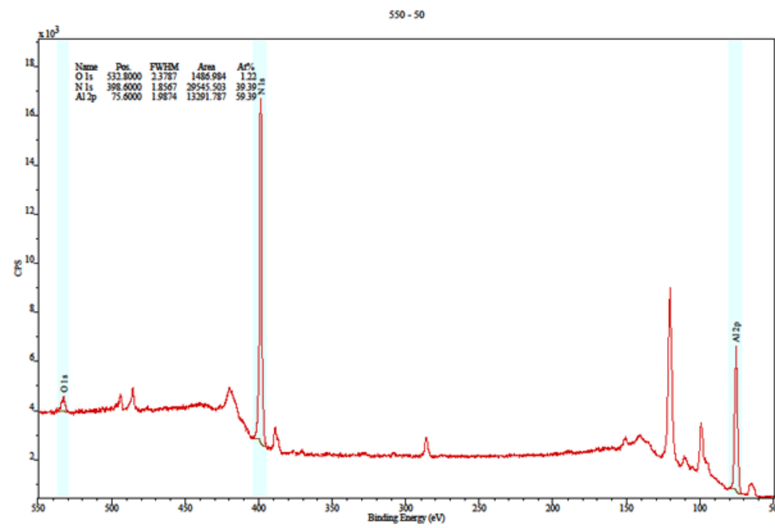

CasaXPS (This string can be edited in CasaXPS.DEF/PrintFootNote.txt)

Figure 27: XPS of AlN on Sapphire

4.4 Network Analyzer Measurements of E-beam Evaporated Samples

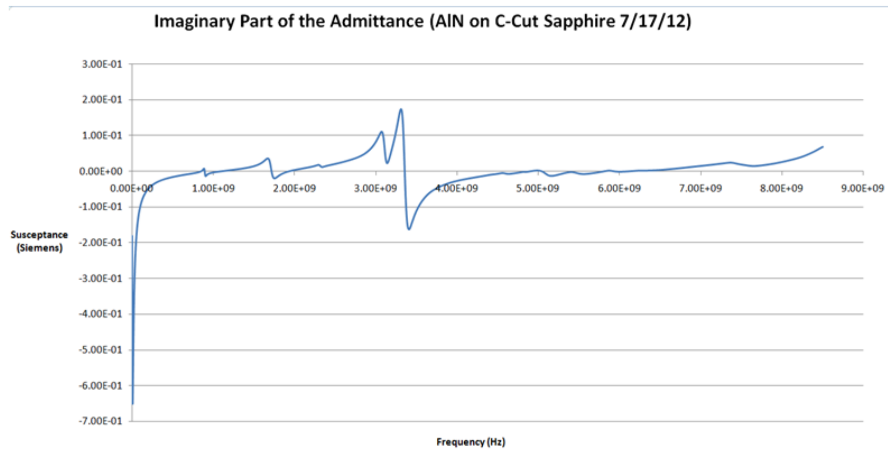

Figure 28: Susceptance of AlN on Sapphire

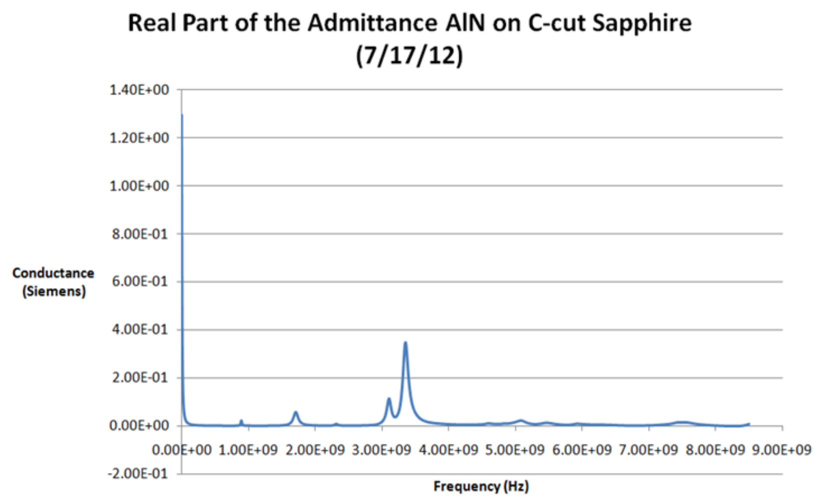

Figure 29: Conductance of AlN on Sapphire

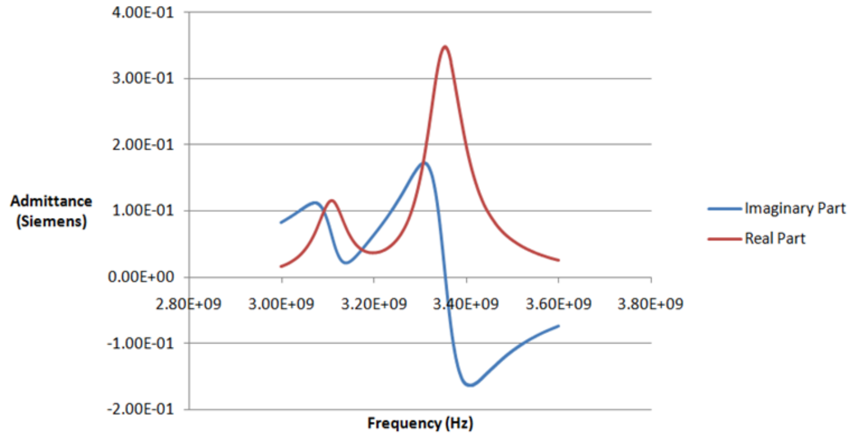

Figure 30: Zoomed Real and Imaginary Parts of the Admittance of AlN on Sapphire

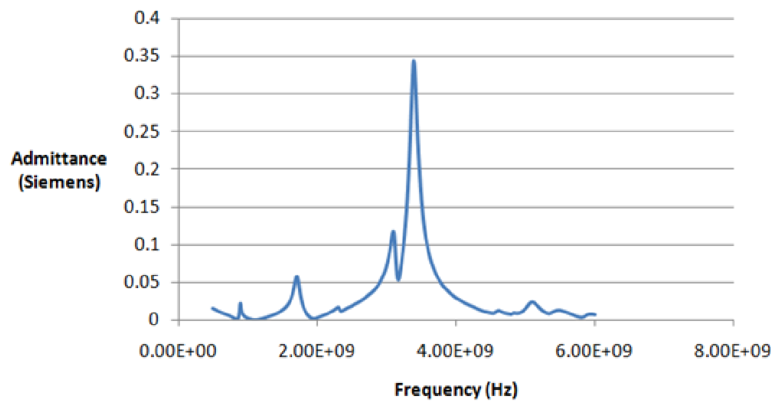

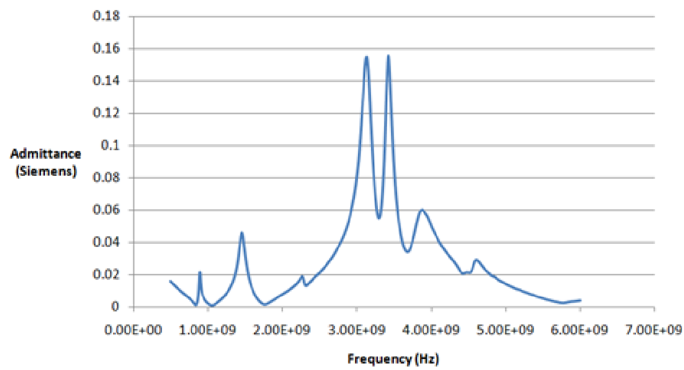

Figure 31: Water on Edges

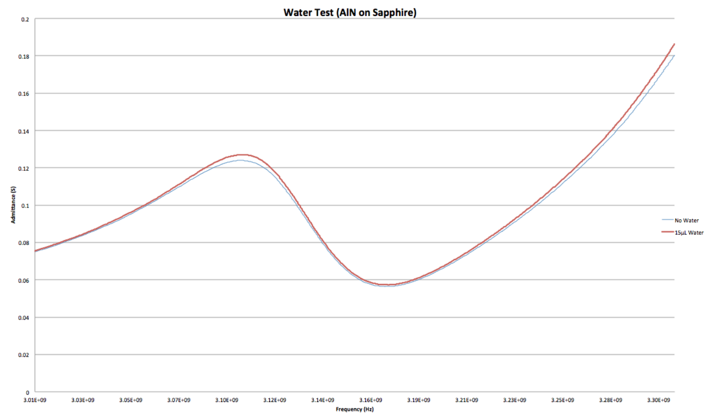

Figure 32: Water Test

5 Discussion

5.1 RF Magnetron Sputtering

Figs. 17-20 show x-ray diffraction data of AlN films. Increasing the substrate temperature from 300°C to 400°C improved the magnitude of the (002) reflection. This result can be explained by a higher amount of kinetic energy given to atoms arriving on the substrate. As we increased the temperature to 550°C, a noticeable decrease in quality occurred. The (002) peak became less intense, whereas others (such as the (102) peak) became more intense. An explanation could be outgassing. Matter often contains frozen or trapped gases inside which can be released upon heating. These released gases could have increased the pressure in the chamber, degrading the film quality. A solution to outgassing would be to monitor the gas pressure (using an ion gauge). Typically one would see a noticeable increase in pressure. Waiting for the chamber to reach the desired base pressure and then sputtering would counteract this effect. The growth rate for Figs. 17-20 reached around 2.5 angstroms per second. Instead of focusing on varying temperature, we decided to take the "best" temperature (400°C) and change the growth rate. Altering the power supply from pulsed DC to RF and using one target at 300W instead of two at 900W each decreased the growth rate to .3 angstroms per second. As one can see, only the (002) peak appears, indicating that the sputtered atoms had enough time to rearrange themselves into the states they wanted. Apparently, the system parameters donated enough energy to the AlN species to encourage c-axis growth. Fig. 21 depicts a pole figure centered on the 002 angle (around 35°). Ideally one would want to see a sharp peak in the center of the graph. However, the broadness of the peak indicates that some grains possess a tilt from the c-axis. Indeed, some grains on the edges could be tilted by some angle, but on the whole the film remains dominantly c-axis. Moreover, the FWHM of this film was around 21°. A singularly oriented film (such as single-crystal epitaxial) has an advantage for sensing applications because the other orientations can lead to piezoelectric cancelling due to symmetry in certain directions. Network analyzer data could not be obtained due to connection issues. Devices

made with a bitewing GS configuration did not coincide with probe tips attached to a Cascade Probe Station. Wire-bonding a SAW device (broken in two in an attempt to eliminate the SAW signal) to an FBAR allowed for a connection because the pattern of the SAW device matches the 3-point probe. These probes were hooked up to an Agilent Network Analyzer. However, upon measurement, only the SAW signal appeared. Perhaps the films were not piezoelectric due to oxygen contamination or poor structure, or the probe station could only connect to the SAW device.

The FWHM of the samples in Figs. 22-23 was around 12°. This is an improvement over previous attempts (21°), but there is much room for improvement. Using the network analyzer and the Cascade Probe Station, we see a weak resonance of very poor quality (due to its bandwidth) at the expected value of 3.06 GHz (Figs. 22-23). To promote acoustic scattering of unwanted modes, we used a photoresist pen to apply photoresist to the back of the device. This cleaned up the signal considerably, but the resonance was still of poor quality (Fig. 24). In addition, the signal had variable quality based on where the probes touched the electrode surface, indicating perhaps non-uniformity. Fitting the data from the absorber measurements to the BVD circuit yielded a Q of about 4. The poor crystal quality of sputtered AlN, coupled with the very low deposition rate of .02 nm per second, encouraged the pursuit of other techniques.

5.2 E-beam Evaporation

Using e-beam evaporation yielded much more success in terms of crystal quality than sputtering. This time, c-cut sapphire and fused silica were used as substrates. Four samples were obtained, two without electrodes (one of each substrate), and two with buried electrodes under the AlN (one of each substrate). Unsurprisingly, the FWHMs for AlN on c-cut sapphire (a template for c-axis growth) were much lower than on fused silica (amorphous). The diffraction scan pictured in Fig. 25 is a log scale with other peaks corresponding to the Al electrodes and the sapphire. Other diffraction scans are not pictured because the only device tested with a network analyzer was the AlN film on sapphire with electrodes. The films on c-cut sapphire and fused silica obtained min-

imum FWHMs of 1.5° and 7.5°, respectively. Furthermore, XPS data revealed the films possessed about 1% oxygen (Fig. 27). However, since XPS is very surface sensitive, the results might not truly reflect the actual composition even if the analysis was carried out *in situ*.

Network analyzer measurements were conducted in air and water for these devices (Figs. 28-30). Data could not be obtained for the fused silica because the metal electrodes were discontinuous at the ends. However, for the sapphire device, the electrodes were bonded to a copper PCB board and connected to the network analyzer using an SMA connector. These data showed numerous resonances, including one at the expected fundamental resonance. These other resonances could be reflections off of the sapphire or could be other modes excited. For a water test, a pipet was used to deposit 15μL of water in 5μL increments (Fig. 32). Since the magnitude of the main resonance did not decrease, and the frequency shifted 795kHz with a resolution of 20001 points/300MHz, a pure shear mode was excited. This mode had a Q of 33 in air, and 36 in water, which is reasonable given the accuracy of the machine. Thus, high quality c-axis AlN was grown on sapphire which can excite the transverse shear mode.

During one of the water tests, water spilled on the substrate (Fig. 31). The most noticeable resonance decreased in magnitude significantly, indicating that the resonance resulted from the sapphire and was not shear. At DC levels, the data shows that the films are conducting. To confirm this, a multimeter was used with the probes touching the AlN, which then signaled that the film was conductive.

6 Conclusions

The practicality of an AlN device has been explored through theoretical and experimental lenses. Finite element modeling determines that AlN devices can operate under lateral field excitation, and resonant under certain frequencies. Theoretical analysis of the Christoffel equation shows that the shear mode can be excited with a lateral field in any direction normal to the c-axis. AlN thin films were fabricated with substrates of borosilicate glass, fused silica, silicon, and r-cut sapphire. The physical deposition methods included reactive magnetron sputtering and e-beam evaporation. Although reactive magnetron sputtering could achieve c-axis AlN, the FWHM of the devices were not ideal. On the other hand, e-beam evaporation produced AlN with FWHMs of around $1.5°$. Using a network analyzer, the shear mode was successfully excited.

7 Future Work

7.1 Crystallinity

Improving the crystallinity of the AlN films can be achieved in numerous ways. Bjurstrom, Wingqvist, and Katardjiev (2006) have used a seed layer to improve the crystallinity as well as create a c-axis tilt in a two-stage deposition process. The first stage consists of a very thin deposited layer (seed layer) at a high process pressure. This high pressure ensures that the Al atoms experience energy losses due to collisions, which allows nucleation on many planes and has a high surface roughness. Lowering the process pressure for a more normal layer is then carried out, which undergo a competitive growth regime (the fastest growing planes overcome the slower ones). Because of the surface roughness, the second layer confined to growing with a c-axis tilt occurs because of the flux from the incoming atoms (Wingqvist, 2009). Seed layers also can act as bottom electrodes for TFE devices, such as Ti or Mo. Ti increases drastically the crystallinity, and has found application in integrated circuit technology (Tran, Schellvis, Pham, Shen, & Sarro, 2010). Furthermore, decreasing the base pressure by means of gettering or backheating can increase the crystallinity by decreasing defects such as oxygen contamination. Thankfully, in air bulk oxidation of AlN occurs only at very high temperatures (1200°C) ("Aluminum Nitride," n.d.), so thereby restricting oxygen concerns to the deposition. Literature indicates that an increase in oxygen also can change the polarity of the film (Akiyama, Kamohara, Kano, Teshigahara, & Kawahara, 2008). Furthermore, AlN films for sensing applications necessitate an oxygen level of 7 at.

7.2 Electrode Configuration

The electrode material, gap length, and shape can be simulated through COMSOL Multiphysics to determine the optimal configuration. Due to impedance matching, the electrode material is important when compared to the piezoelectric material. Moreover, the gap length can either strengthen or weaken the electric field, which affects the energy

density. The shape of the electrodes can alter edge effects or increase or decrease the active area of the sensor. In any case, these three parameters are important for a successful sensor.

7.3 Minimizing Acoustic Interference

Two main structures have been developed for the minimization of acoustic interference, the Bragg reflector (solidly mounted resonator) or an air-backed resonator (free-standing membrane). The Bragg reflector consists of a stack of quarter wavelength layers of low and high impedances (S.H. Kim, J.H. Kim, J.K. Lee, S.H. Lee, & Yoon, 2000). When an acoustic wave delves into the substrate, acoustic energy losses occur. This configuration allows the wave to constructively interfere, essentially reflecting the wave back and minimizing the impedance of the substrate. Generally, fabrication remains straightforward in the lateral field excitation case, where the layers can be deposited using magnetron sputtering. On the other hand, an air-backed resonator creates an aircavity underneath the device, which reflects the acoustic energy. Membrane structures, more fragile than solidly mounted resonators, typically receive better coupling coefficients and quality (Zhang & Kim, 2002). However, some devices have been fabricated that can withstand a 1 meter fall, (Zhang & Kim, 2002), a promising result in terms of practicality. Fabrication includes a more complicated procedure, but can be carried out using a sequence of dry and wet etching. This sequence (Bjurstrom et al., 2006) includes depositing and patterning the bottom electrode with wet etching. A layer of Ni as an etch stop (to stop etching from occurring in later stages) is deposited and patterned using liftoff. Depositing the piezoelectric film and patterning using reactive ion etching creates holes to contact the bottom electrode and for sample injection. Furthermore, the top electrode is deposited and patterned as well as electrode pads. To create a “microfluidic channel, Al is on the backside of the device, and patterned it for the channel system. Aside from energy losses, isolating the thin film from the substrate can decrease the amount of modes excited due to imperfections in the substrate. Acoustic resonators based on silicon, with dimensions in the micron range, are called micro

electro-mechanical systems (MEMS).

7.4 Stress

Stress becomes a huge role in AlN thin films. Large amounts of residual stress may be present from thermal stress during deposition that has not relaxed, or a lattice mismatch with the substrate. For MEMS devices, the stress has to be zero or tensile, otherwise it will buckle and the device will be unusable. Using x-ray diffraction or wafer bow measurements, the stress can be measured. If the stress were compressive,then an attached layer of tensile stress of the same magnitude can cancel it out. Stress can also be reduced by an AlN buffer (Huttel, Gomez, Cebollada, Armelles, & Alonso, 2002), using an alloy layer (Edgar et al., 2002), adjusting deposition conditions (Si-Hyung Lee, Yoon, Cheong, & Jeon-Kook Lee, 2003; Tang, Jaing, Kun-Hsien Lee, & Cheng-Chung Lee, (2003), among other methods. In any case, stress needs to be taken seriously as it can affect the piezoelectric properties of AlN.

7.5 CMOS Integration

CMOS circuits are integrated circuits. Three common techniques are used: Hybrid, monolithic, and heterogeneous. Monolithic integration is a technique where an integrated circuit is combined with a MEMS on the same substrate, and seems to be the best choice for this project. In this case, the MEMS structure can be built on top of a CMOS substrate through micromachining techniques. An advantage of this technique concerns the reduction of parasitic effects of connecting MEMS with CMOS due to the presence of holes to shorten the connections. Unfortunately, all processes must be CMOS compatible; that is, the process temperatures cannot exceed 400°C. A good overview of this subject can be found in Campanella (2010). This technique offers the ability to build sensor arrays, where each sensor individually measures a different measurand. Measurements can be observed through a readout due to the integrated circuit, which in the ideal case would enable rapid detection of many different types of biomarkers.

8 References

Abad, J. M., Pariente, F., Hernandez, L., Abruna, H. D., & Lorenzo, E. (1998). Determination of organophosphorus and carbamate pesticides using a piezoelectric biosensor. *Analytical Chemistry, 70*(14), 2848-2855.

Akiyama, M., Kamohara, T., Kano, K., Teshigahara, A., & Kawahara, N. (2008). Influence of oxygen concentration in sputtering gas on piezoelectric response of aluminum nitride thin films. *Applied Physics Letters, 93*(2), 021903-021903.

Aluminium Nitride. (2011). Retrieved August 19, 2011, from http://en.wikipedia.org/wiki/Aluminium_nitride

Auld, B. A. (1973). *Acoustic fields and waves in solids* (Vol. 1). New York: Wiley.

Ballato, A., Hatch, E. R., Mizan, Muhammad, & Lukaszek, T. J. (1986). Lateral field equivalent networks and piezocoupling factors of quartz plates driven in simple thickness modes. *IEEE Transactions on Ultrasonics Ferroelectrics and Frequency Control, 33*, 385-393.

Baraton, M. I. (Ed.). (2009). *Sensors for environment, health and security.* Springer.

Berkenpas, E., Millard, P., & Pereira da Cunha, M. (2006). Detection of *Escherichia coli* O157: H7 with langasite pure shear horizontal surface acoustic wave sensors. *Biosensors and Bioelectronics, 21*(12), 2255-2262.

Bjurstrom, J., Wingqvist, G., & Katardjiev, I. (2006). Synthesis of textured thin piezoelectric AlN films with a nonzero C-axis mean tilt for the fabrication of shear mode resonators. *Ultrasonics, Ferroelectrics and Frequency Control, IEEE Transactions on, 53*(11), 2095-2100.

Bronzino, J. D. (Ed.). (2000). *The biomedical engineering handbook. 2* (Vol. 2). CRC press.

Campanella, Humberto. (2010). *Acoustic Wave and Electromechanical Resonators: Concept to Key Applications* (Vol. 1). Boston: Artech House.

Carter, R. M., Mekalanos, J. J., Jacobs, M. B., Lubrano, G. J., & Guilbault, G. G. (1995). Quartz crystal microbalance detection of *Vibrio cholerae* O139 serotype. *Journal of immunological methods, 187*(1), 121-125.

Chen, D., Wang, J., Li, D., Xu, Y., & Li, Z. (2011). Solidly mounted resonators operated in thickness shear mode based on *c*-axis oriented AlN films. *Sensors and Actuators A: Physical, 165*(2), 379-384.

Cooper, M. A., & Singleton, V. T. (2007). A survey of the 2001 to 2005 quartz crystal microbalance biosensor literature: applications of acoustic physics to the analysis of biomolecular interactions. *Journal of Molecular Recognition, 20*(3), 154-184.

Corso, C. D., Dickherber, A., & Hunt, W. D. (2007). Lateral field excitation of thickness shear mode waves in a thin film ZnO solidly mounted resonator. *Journal of*

Applied Physics, 101(5), 054514-054514.

Dubois, M. A., & Muralt, P. (1999). Properties of aluminum nitride thin films for piezoelectric transducers and microwave filter applications. *Applied Physics Letters, 74*(20), 3032-3034.

Dumitru, V., Morosanu, C., Sandu, V., & Stoica, A. (2000). Optical and structural differences between RF and DC Al_xN_y magnetron sputtered films. *Thin Solid Films, 359*(1), 17-20.

Edgar, J. H., Liu, L., Liu, B., Zhuang, D., Chaudhuri, J., Kuball, M., & Rajasingam, S. (2002). Bulk AlN crystal growth: self-seeding and seeding on 6H-SiC substrates. *Journal of crystal growth, 246*(3), 187-193.

French, L. A., McCann, D. F., Wark, M., Winters, S., & Vetelino, J. F. (2007, June). A lateral field excited acoustic wave sensor. In *Solid-State Sensors, Actuators and Microsystems Conference, 2007. TRANSDUCERS 2007. International* (pp. 1287-1290). IEEE.

Fu, Y. Q., Luo, J. K., Du, X. Y., Flewitt, A. J., Li, Y., Markx, G. H., ... & Milne, W. I. (2010). Recent developments on ZnO films for acoustic wave based biosensing and microfluidic applications: a review. *Sensors and Actuators B: Chemical, 143*(2), 606-619.

Guenther, K. H. (1990, December). Revisiting structure-zone models for thin-film growth. In *San Dieg-DL Tentative* (pp. 2-12). International Society for Optics and Photonics.

Hamamatsu, S. (1993). New biosensor using shear horizontal surface acoustic wave device. *Jpn. J. Appi. Phys. Vol, 32,* 2376-2379.

Hansen, K. M., & Thundat, T. (2005). *Microcantilever biosensors. Methods, 37*(1), 57-64.

Hatch, E. R., & Ballato, A. (1983). Lateral-field excitation of quartz plates. In 1983 *Ultrasonics Symposium* (pp. 512-515). IEEE.

Hempel, U., Lucklum, R., Vetelino, J. F., & Hauptmann, P. (2008). Advanced application of the impedance spectrum of a lateral field excited sensor. *Sensors and Actuators A: Physical, 142*(1), 97-103.

Homola, J. (2008). Surface plasmon resonance sensors for detection of chemical and biological species. *Chemical reviews, 108*(2), 462-493.

Hu, Y., Pinkham, W., French Jr, L. A., Frankel, D., & Vetelino, J. F. (2005). Pesticide detection using a lateral field excited acoustic wave sensor. *Sensors and Actuators B: Chemical, 108*(1), 910-916.

Huttel, Y., Gomez, H., Cebollada, A., Armelles, G., & Alonso, M. I. (2002). Epitaxial growth of AlN on sapphire (0001) by sputtering: a structural, morphological and optical study. *Journal of crystal growth, 242*(1), 116-123.

Katardjiev, I., & Yantchev, V. (2012). Recent developments in thin film electro-acoustic

technology for biosensor applications. *Vacuum, 86*(5), 520-531.

Keiji Kanazawa, K., & Gordon II, J. G. (1985). The oscillation frequency of a quartz resonator in contact with liquid. *Analytica Chimica Acta, 175,* 99-105.

Kim, S. H., Kim, J. H., Lee, J. K., Lee, S. H., & Yoon, K. H. (2000). Bragg reflector thin film resonator using aluminium nitride deposited by RF sputtering. In *Mi crowave Conference, 2000 Asia-Pacific* (pp. 1535-1538). IEEE.

Kondoh, J., Matsui, Y., Shiokawa, S., & Wlodarski, W. B. (1994). Enzyme-immobilized SH-SAW biosensor. *Sensors and Actuators B: Chemical, 20*(2), 199-203.

Landau, L. D., & Lifshitz, E. M. (1959). *Course of Theoretical Physics Vol 7: Theory and Elasticity.* Pergamon Press.

Larson III, J. D., Bradley, P. D., Wartenberg, S., & Ruby, R. C. (2000, October). Modified Butterworth-Van Dyke circuit for FBAR resonators and automated measurement system. In *Ultrasonics Symposium, 2000 IEEE* (Vol. 1, pp. 863-868). IEEE.

Lee, S. H., Hyun Yoon, K., Cheong, D. S., & Lee, J. K. (2003). Relationship between residual stress and structural properties of AlN films deposited by rf reactive sputtering. *Thin Solid Films, 435*(1), 193-198.

Mason, W. P. (1950). *Piezoelectric crystals and their application to ultrasonics.* Van Nostrand Reinhold.

Morkoc, H. (1999). *Nitride semiconductors and devices* (Vol. 32). Springer.

Mullis, K. B., & Faloona, F. A. (1987). Specific synthesis of DNA in vitro via a polymerase-catalyzed chain reaction. *Methods in enzymology,* 155, 335.

n.d. ELISA. Retrieved from http://en.wikipedia.org/wiki/ELISA.

n.d. History of Piezoelectricity. Retrieved from http://www.piezo.com/tech4history.html.

Nye, J. F. (1957). Physical Properties of Cristals: Their Representation by Tensors and Matrices. Oxford University Press.

Pinkham, W. A. (2007). A lateral field excited acoustic wave pesticide sensor.

Polanski, M., & Anderson, N. L. (2006). A list of candidate cancer biomarkers for targeted proteomics. *Biomarker Insights, 1*, 1.

Properties of Typical Aluminum Nitride Substrates. (2012). Retrieved from http://www.edgepolishing.com/aluminum-nitride.htm

Rosenbaum, J. F. (1988). *Bulk acoustic wave theory and devices* (Vol. 1). Boston: Artech House.

Satoh, Y., Ikata, O., Miyashita, T., & Ohmori, H. (2001, March). RF SAW Filters. In *International Symposium on Acoustic Wave Devices for Future Mobile Communication Systems* (pp. 125-132).

Sauerbrey, G. Z. (1959). Use of quartz vibration for weighing thin films on a microbalance. *J. Physik, 155*, 206-212.

Tang, C. J., Jaing, C. C., Lee, K. H., & Lee, C. C. (2011). Optical properties and residual stress in aluminum nitride films prepared by alternating-current dual reactive magnetron sputtering. *Applied Optics, 50*(13), 1945-1950.

Thin Film BAW Resonator. Retrieved from www.comsol.com/model/download/38331/thin_film_baw_resonator.pdf

Thornton, J. A. (1977). High rate thick film growth. *Annual review of materials science,* 7(1), 239-260.

Tiersten, H. F. (1969). *Linear piezoelectric plate vibrations: Elements of the linear theory of piezoelectricity and the vibrations of piezoelectric plates.* Plenum Press.

Tran, A. T., Schellevis, H., Pham, H. T. M., Shen, C., & Sarro, P. M. (2010). Influence of seed layer on crystallinity and orientation of pulsedDC sputtered AlN thinfilms for piezoelectric actuators. *Procedia Engineering, 5*, 886-889.

Van Weemen, B. K., & Schuurs, A. H. W. M. (1971). Immunoassay using antigen-enzyme conjugates. *FEBS letters, 15*(3), 232-236.

Vergara, L., Clement, M., Iborra, E., Sanz-Hervas, A., Garca Lpez, J., Morilla, Y., ... & Respaldiza, M. A. (2004). Influence of oxygen and argon on the crystal quality and piezoelectric response of AlN sputtered thin films. *Diamond and related materials, 13*(4), 839-842.

Vetelino, J., & Reghu, A. (2010). *Introduction to sensors.* CRC Press.

Wang, L., Wei, Q., Wu, C., Hu, Z., Ji, J., & Wang, P. (2008). The Escherichia coli O157: H7 DNA detection on a gold nanoparticle-enhanced piezoelectric biosensor. *Chinese Science Bulletin, 53*(8), 1175-1184.

Wark, M., Kalanyan, B., Ellis, L., Fick, J., Connell, L., Neivandt, D., & Vetelino, J. F. (2007, October). P0-9 a lateral field excited acoustic wave sensor for the detection of saxitoxin in water. In *Ultrasonics Symposium, 2007. IEEE* (pp. 1217-1220). IEEE.

Wingqvist, G. (2009). *Thin film electroacoustic devices for biosensor applications* (Doctoral dissertation, Uppsala University).

Wingqvist, G. (2010). AlN-based sputter-deposited shear mode thin film bulk acoustic resonator (FBAR) for biosensor applicationsa review. *Surface and Coatings Technology, 205*(5), 1279-1286.

Xu, X. H., Wu, H. S., Zhang, C. J., & Jin, Z. H. (2001). Morphological properties of AlN piezoelectric thin films deposited by DC reactive magnetron sputtering. *Thin Solid Films, 388*(1), 62-67.

Zampolli, M., Malm, N., & Tesei, A. (2008, November). Improved Perfectly Matched Layers for Acoustic Radiation and Scattering Problems. In *Proceedings of the*

COMSOL Conference.

Zhang, H., & Kim, E. S. (2002). Air-backed Al/ZnO/Al film bulk acoustic resonator without any support layer. In *Frequency Control Symposium and PDA Exhibition, 2002. IEEE International* (pp. 20-26). IEEE.

Zhu, J., Zhao, D., Luo, W. B., Zhang, Y., & Li, Y. R. (2008). Epitaxial growth of cubic AlN films on $SrTiO_3$ (100) substrates by pulsed laser deposition. *Journal of Crystal Growth, 310*(4), 731-737.

A Tensors and Indicial Notation

Tensors extend the ideas of scalars and vectors to quantify information about a physical system. Scalars, often referred to as tensors of rank zero, convey the magnitude of some quantity. Vectors portray the magnitude and direction of some quantity, and are known as tensors of rank one. Tensors of rank two consist of an array of components. These tensors can be mathematically represented as matrices, identifying information on the magnitude, direction, and planes on which components act. The number of components in a tensor is given by m^n, where m refers to the dimension of the space (three spatial dimensions for this thesis) and n corresponds to the rank of the tensor. As an example, the tensor fields of stress and strain assign a tensor of stress or strain to every point in space, and consist of $3^2 = 9$ components.

Consider two vectors **A** and **B** in a vector space with a basis $\{e_i\}$. The dot product between two three-dimensional vectors is given by:

$$\mathbf{A} \cdot \mathbf{B} = \sum_{i=1}^{3} A_i B_i = A_i B_i, \tag{A.1}$$

where summation over the dummy index i (or dummy indices) is assumed henceforth. The vector cross product may be written as:

$$\mathbf{A} \times \mathbf{B} = \epsilon_{ijk} A_i B_j e_k \tag{A.2}$$

where ϵ_{ijk} is defined as the Levi-Cevita symbol and takes on values of +1 if the indices i, j, k is a cyclic permutation of 1,2,3, 0 if any indices are the same, and -1 if the indices are anticyclic.

The spatial gradient operator assigns the spatial derivative of a scalar field to each corresponding direction in a vector. The gradient of a vector is a tensor of rank two. These definitions extend to the divergence and curl of some vector field **A**:

$$\nabla \cdot \mathbf{A} = \frac{\partial A_i}{\partial x_i} = A_{i,i} \text{ and } \nabla \times \mathbf{A} = \epsilon_{ijk} e_i A_{k,j} \tag{A.3}$$

A.1 Tensor Transformations

Consider two sets of Cartesian axes (Ox, Oy, Oz) and (Ox', Oy', Oz') with the same origin. A point P has the coordinates:

$$x' = l_1x + m_1y + n_1z, \quad y' = l_2x + m_2y + n_2z, \quad z' = l_3x + m_3y + n_3z \tag{A.4}$$

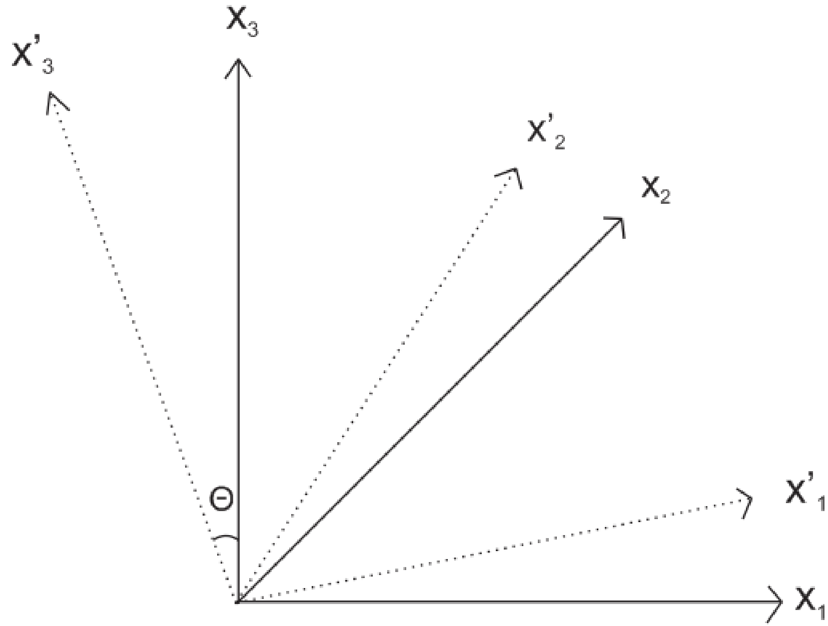

Figure 33: Rotated Coordinate System

when relating one set of axes to another. The quantities $(l_1, \ldots, n_3)$ are called the direction cosines. We can rewrite equation (A.4) as:

$$x'_j = a_{1j}x_1 + a_{2j}x_2 + a_{3j}x_3 = \sum_{i=1}^{3} a_{ij}x_i = a_{ij}x_i \tag{A.5}$$

by convention. By geometry, direction cosines can be rewritten as:

$$a_{ij} = \frac{\partial x'_j}{\partial x_i} \tag{A.6}$$

A tensor of the second rank can be the product of two vectors, thus it can be transformed as the product of two direction cosines:

$$x'_j x'_l = \frac{\partial x'_j}{\partial x_i} \frac{\partial x'_l}{\partial x_k} x_i x_k \tag{A.7}$$

In full generality, the transformation equation for an nth ranked tensor is:

$$X'_{k_1 \ldots k_n} = \frac{\partial x_{k'_1}}{\partial x_{j_1}} \frac{\partial x_{k'_2}}{\partial x_{j_2}} \cdots \frac{\partial x_{k'_n}}{\partial x_{j_n}} X_{j_1 \ldots j_n} \tag{A.8}$$

9 Author's Biography

Michael Robert FitzGerald was born September 30th, 1990 in Topsham, Maine. He is a dual-degree candidate in physics and mathematics from The University of Maine in August, 2013. He is a member of the physics honors society Sigma Pi Sigma. He has received numerous scholarships and participated in the National Science Foundation sponsored program Research Experience for Undergraduates. Upon graduation, Michael plans to obtain a position in the semiconductor industry.